Energy inputs and upward motion in the cusp

Åsmund Steen Skjæveland

April 19, 2017

Thesis submitted for the degree of Philosophiæ Doctor

Contents

List of Figures

List of Tables

Acknowledgments

This thesis has been a rather longer step than I intended in this journey of mine. When it began is hard to say. Perhaps when I first saw the northern lights. Perhaps when, as a young student, I found out it was possible to get an education while staring at the sky. And so I set out to look at northern lights. I looked at them, very hard, through narrow-band optical filters, radar beams, computer screens, equations and figures, occasionally glancing away and up to once again be caught and transfixed by those swirling, dancing, otherworldly curtains of light, every time more beautiful for understanding them better.

Here we are, after many stumbles; the thesis is done. I owe great thanks to those whose love, encouragement and understanding have pushed me along. There are of course my supervisors and co-authors Herb and Jøran who often had much more faith in me than I had myself; my parents and family who have always encouraged, supported and helped me; my study mates, particularly Pål and Siri, and Joachim and Lise; the Biørneblæs orchestra, where I had great fun and parties abusing a clarinet and singing silly songs many of these years; and not least my wife Øyonn, who has often carried me on her back these last few years.

Without you, no thesis. Thank you.

Abstract

The energy deposition in the cusp by dayside reconnection is a significant driver of bulk vertical motion in the cusp plasma. The small size of the cusp belies its importance in solar wind-Earth interaction. Ion heating drives and enhances plasma upflows which feed the outflow processes in the topside ionosphere, populating the magnetosphere with hot heavy ions. Netural heating causes local thermospheric upwelling which greatly modifies the neutral density and composition. Precipitating electrons change the electron density (n_e) profile, steering the neutral heating to the altitudes where it is most effective in causing upwelling. This thesis investigates: the structure of cusp ion upflows and their response to electron (T_e) and ion (T_i) temperature enhancements in detail, and their relation to dayside auroral forms; the ion number flux in ion upflows and their ability to feed outflow processes; and the occurrence rate of ion heating events in the cusp and the realistic temperature and electron density profiles in the dark cusp both when reconnection-enhanced and quiescent.

The strongest upflows were observed when both T_i and T_e were enhanced. T_i were most enhanced near the edges of poleward moving auroral forms (PMAFs). These upflows can easily transport plasma from 600 km altitude to 800 km altitude, where nonthermal energization mechanisms can create ion outflows. Plasma from lower altitudes is not likely to be fed into upflows, but the region between ~400–500 km is drained of plasma to replace that lost from higher altitudes. The electron densities and ion temperatures in the lower F region during reconnection events are very different from those predicted by the MSIS and IRI models. Particularly the IRI model n_e profile is less than our empirical observations of the dark (non-sunlit) cusp n_e by a factor 10–30, and it is not suitable for model studies of cusp energy deposition. We present statistical profiles of n_e and T_i for the quiescent and reconnection-enhanced states to fill this void.

In sum, this thesis increases our knowledge of the processes that drive vertical transport of plasma and neutral gas in the cusp.

Chapter 1

Introduction

The topic of this thesis is the reconnection-powered heating and upward transport of plasma and neutral gas in the ionospheric cusp. This is a matter of scientific interest as the cusp and cleft is a highly dynamic region which is important regarding escape of plasma from the ionosphere into the magnetosphere, as well as the dynamic composition of the cusp thermosphere. In addition, this is also important to spaceflight. Earth-observing satellites in a low polar orbit, and the repeated upwelling-driven neutral density enhancement in the cusp significantly increases local satellite drag, potentially shortening the orbital lifetime of spacecraft that cross the cusp at low altitudes. Magnetic reconnection between the interplanetary magnetic field (IMF) and the Earth's magnetic field injects large amounts of energy into the magnetosphere and cusp ionosphere, causing strong vertical motion of ionized and neutral gas.

Pulsed ion upflow, strong near-vertical winds of ionospheric plasma, occur along the auroral oval, and are an important feature of the ionospheric cusp. Ion upflow in the cusp is closely linked to the transfer of energy from the solar wind to the magnetosphere and ionosphere through magnetic reconnection on the magnetosphere front.

These pulses of near-vertical plasma wind, lasting only a few minutes each, are driven by heating of the ionospheric plasma, and will lift heated plasma tens to hundreds of km to altitudes where non-thermal processes can accelerate a small portion of the gas further upward, often into the magnetosphere. A significant portion of O^+ ions lost to space escape this way via cusp outflows.

When the ionospheric plasma is heated, the neutral gas is also heated. Depending on the altitude of heating, the effect can be dramatic. The neutral gas expands and lifts the atmospheric column upward, significantly increasing the

neutral density and changing the neutral composition up to at least 400 km altitude.

This thesis addresses three science questions:

1. What are the major drivers for cusp ion upflows?
2. Which cusp upflows can reach outflow energization altitudes?
3. What are the actual energy deposition rates in the dynamic cusp?

To answer these questions, I have chosen an experimental approach using ground instrumentation. Svalbard is ideally located underneath the dayside cusp and cleft aurora. Around midwinter it is dark enough at noon to observe very faint aurora from the ground. This makes Svalbard an ideal location from which to examine dayside aurora with optical methods. I combine optical observation with incoherent scatter radar (ISR) data from the EISCAT Svalbard Radar (ESR). The radar data I use is available from the EISCAT web site. The ISR technique allows for direct observation of basic plasma parameters (density, temperature, line-of sight velocity) with good spatial and temporal resolution. I apply fairly fundamental physics to the observations, guided by pre-existing theory of transient heating and flow bursts, when analysing the observations. The cusp is not yet exhaustively studied, and there is much yet to learn from such relatively basic methods. My three papers attempt to answer the three questions above. The papers examine basic plasma parameters in different ways.

Paper 1 takes advantage of a transit of the dayside auroral oval across the ESR beam while the aurora is active, and several upflows are seen. This is an event-driven case study, where I examine individual upflow and auroral events as they pass across the radar beam at different times in their evolution. I use the simultanteous optical and radar data to look at simultaneous upflow and heating event by event, and how it relates to transient auroral forms, and under which conditions we see the strongest plasma heating and upflows.

For paper 2 I expand on the data set analyzed in paper 1. A long sequence of ion upflows allows a statistical approach. First I describe the general features of the observed upflows, then I analyze the body of data as a whole to see how the number flux density of upflowing ions relates to plasma temperatures. I then show how far upflowing plasma can be uplifted in one event, using three different empirical models for the time evolution of upflow. Finally I present better equations for modelling upflow travel times based on observed characteristics of upflows.

Paper 3 continues the statistical approach. I examine the distribution and occurrence of heating events over a larger portion of the cusp ionosphere, using the ESR in a scanning mode to cover a large area, and using data from three winters. Then I produce empirical model profiles of electron densities (n_e) and ion temperatures (T_i) inside and outside reconnection events. These profiles are then used to produce order of magnitude improvements in estimates of the energy deposition rates in the cusp than can be achieved using average values or statistical models. The improved n_e and T_i profiles combined with the improved heating event statistics will enable significantly more realistic modelling of cusp thermospheric heating, upwelling and satellite drag.

1.1 Thesis organization

Chapters 2 through 5 of this thesis are a brief introduction to the physics of ionospheric plasma and the solar wind-ionosphere connection, as it applies to this thesis, as well as a short description my data sources.

I start out fairly basic and gradually progress to more advanced topics. These chapters are by no means exhaustive or complete, nor do I intend them to be. I only discuss subjects relevant to the phenomena I discuss in the papers, with some extra material where I feel I would not provide the necessary background to a physicist not already introduced to space physics. Still, there are many phenomena in space physics I do not discuss at all because they're not directly relevant to this thesis. Many processes have been greatly simplified in my description. Readers who want to know more may want to consult Kivelson and Russell [1995], Brekke [1997, 2013] or Schunk and Nagy [2009].

After the introduction to basic physics follows a more thorough summary of my work, and finally the three papers.

Part I

Background

Chapter 2

Selected plasma physics topics

This chapter gives a brief introduction to some central plasma physics concepts relevant to this thesis. It is not in any way meant to be exhaustive.

2.1 Simple motion of a charged particle

In addition to gravity, a charged particle moving without collisions is subject to the forces of electricity and magnetism. Imagine a point particle with charge q, mass m, and velocity $\mathbf{v}$, all nonzero. The electric force is straightforward:

$$\mathbf{F}_E = q\mathbf{E} \tag{2.1}$$

where $\mathbf{E}$ is the electric field. The particle will accelerate in the direction of the electric field.

The magnetic force is orthogonal to the direction of motion and the direction of the magnetic field $\mathbf{B}$:

$$\mathbf{F}_B = q(\mathbf{v} \times \mathbf{B}) \tag{2.2}$$

so the magnetic force is always orthogonal to the particle's motion. In a constant magnetic field, charged particles will move in circles. The center of the circle is called the *guiding center*, and the rotational frequency $\Omega_c = qB/m$ (orbits per second) is called the *gyrofrequency*. The radius of the circle is the *gyroradius* $r_c = mv_\perp/qB$, where $v_\perp$ is the component of $\mathbf{v}$ perpendicular to the magnetic field.

If $\mathbf{v}$ has a component parallel to the magnetic field, the particle will move in a helix.

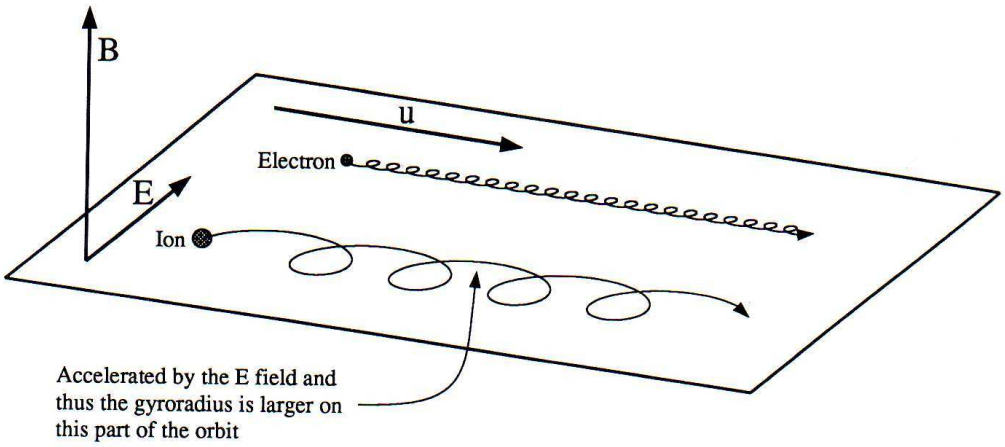

Figure 2.1: Illustration of $\mathbf{E} \times \mathbf{B}$ particle drift. Positive and negative charges drift in the same direction at the same speed independent of mass or charge. From Kivelson [1995].

The electric and magnetic on the particle forces combine to the Lorenz force:

$$\mathbf{F} = m\frac{d\mathbf{v}}{dt} = q\mathbf{E} + q(\mathbf{v} \times \mathbf{B}) \tag{2.3}$$

2.1.1 $\mathbf{E} \times \mathbf{B}$ drift

In the case of $\mathbf{E} \perp \mathbf{B}$ and both fields constant and no other forces present, it can be shown that ions and electrons both will gyrate in a direction perpendicular to both $\mathbf{E}$ and $\mathbf{B}$, and at the same speed. The guiding center will move at a constant velocity

$$\mathbf{v_c} = \frac{\mathbf{E} \times \mathbf{B}}{B^2} \tag{2.4}$$

Since this velocity vector is independent of mass and charge (as long as $q \neq 0$) there is no charge separation and no current caused by this drift. Figure 2.1 illustrates the drift of ions and electrons. Gyroradius and gyrofrequency are mass-dependent, and so the gyrofrequency is much higher and the gyroradius much smaller for electrons than for ions.

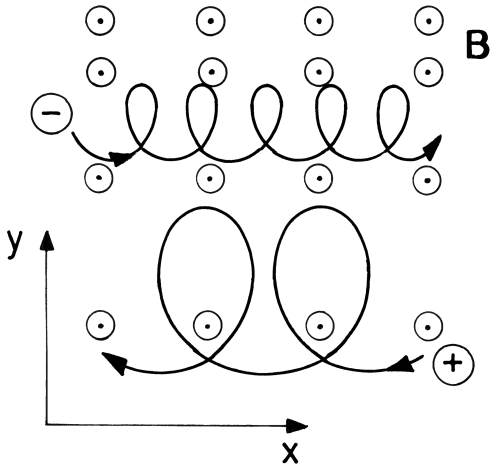

Figure 2.2: Illustration of $\nabla \cdot \mathbf{B}$ particle drift when $\partial B/\partial y \neq 0$. When the particle moves into stronger magnetic field, the $\mathbf{F}_B$ force is stronger, so the gyroradius is smaller and the particle does not return to its original position. Figure from Pécseli [2005].

2.1.2 Gradient drift

If the magnetic field is not constant, gradient drift will occur. When a gyrating charge moves through a gradient in the magnetic field, the gyroradius shrinks and expands as the field gets stronger and weaker. Figure 2.2 illustrates the effect for a gradient in field strength along the Y axis. Since the direction of gyration is charge-dependent, this effect causes positive and negative charges to go in opposite directions, and a current forms. Notably, the *ring current*, a magnetospheric current that circles the Earth near the magnetic equator at 3–6 R_E (see Figure 3.3), is formed by gradient drift.

2.1.3 Magnetic mirroring and bottling

When magnetic field lines are nonparallel, a the magnetic force on a gyrating charge will have a component parallel to the direction of lower flux density. This will act to slow down and reflect incoming charges. Figure 2.3 illustrates the effect, and shows how a charged particle can be trapped in a magnetic field. This trapping of charged particles by the magnetic field is called "magnetic bottling". How deep into the "bottlenecks" the particle travels depends on the particle's kinetic energy and angle of its velocity vector to the magnetic field. The magnetospheric particle may be lost to the ionosphere due to collisions with atmospheric

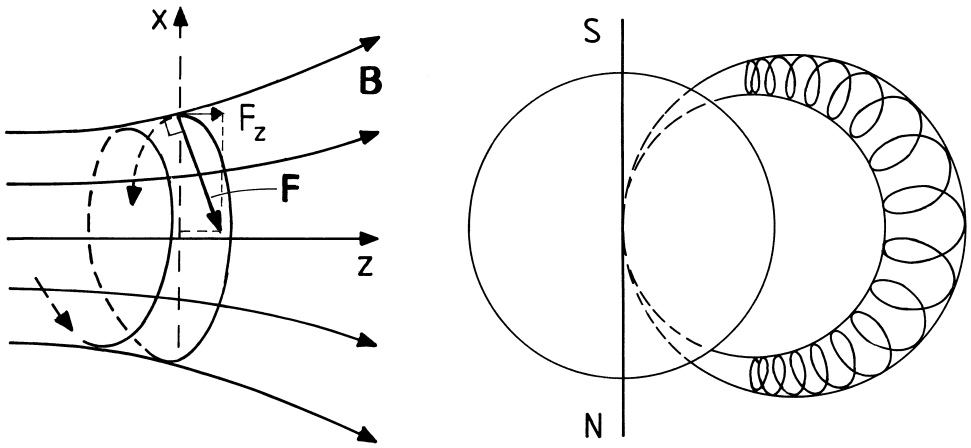

Figure 2.3: Illustration of a magnetic mirror and a bottle particle trap. The left figure shows a magnetic mirror. The $\mathbf{F}_B$ force has a component parallel to the centerline when the magnetic field lines are spreading out, in the direction of lower flux density. The right figure shows how this can trap charges in a dipole-like field, a "magnetic bottle". Figure from Pécseli [2005].

molecules if it penetrates deep enough into the "bottleneck".

2.2 The frozen-in field approximation

A "collisionless plasma" means that the plasma gas is sufficiently rarified that collisions between the particles that make up the plasma can be ignored on relevant time scales and length scales, and only electromagnetic interactions between the particles need be considered. The solar wind and the interstellar medium are examples of collissionless plasmas.

In a collisionless plasma in steady state the electrical conductivity can be approximated as infinite, i.e. the plasma is a superconducting gas. In this case charges cannot move across magnetic field lines because this would induce infinite eddy currents [Alfvén, 1942]. This is the "frozen flux" approximation, in which the plasma is "frozen" to the magnetic field, or vice versa, the field is frozen to the plasma, and moves with the plasma. This approximation is not valid for length scales smaller than the ion gyroradius.

2.2.1 Flux tubes

Magnetic field lines, normally just a visual aid, take on an ephemeral reality as the frozen-in plasma is free to move along the magnetic field lines but not across them. It is possible for relatively nearby plasma volumes on different field lines to have quite different plasma properties. We can imagine such populations, confined by the magnetic field, as independent volumes called *flux tubes*.

A flux tube can be visualized as a cylinder of magnetic flux moving as a unit, carrying frozen-in plasma along. The plasma in the tube is fairly homogeneous but may be distinct from nearby plasma outside the tube. During bursty reconnection (see Section 3.4) flux tubes from different sectors of the magnetosphere may be brought together, creating strong horizontal gradients.

2.3 Collisional plasma

Most of the gas in the upper atmosphere between 100–1000 km is neutral and only a small portion is ionized. Free electrons and ions in the ionosphere will occasionally collide with neutral molecules and atoms, and with other ions and electrons. This is quantified as the *collision frequency*, usually written as ν_{ab} where a and b are particle and target, respectively. For example, ν_{in} is the ion-neutral collision frequency, i.e. how many times per second a single ion will collide with a neutral particle. ν_{O^+O} is the collision frequency of a single O^+ ion colliding with an oxygen atom. The ion-neutral collision frequency depends strongly on neutral density, so it decreases rapidly with altitude, from 100–1000 collisions per second at 100 km altitude to 0.1–1 per second at 300 km.

The ion-ion, ion-electron and electron-neutral collision frequencies are much smaller than the ion-neutral frequency in the regions I study, so I will not go into them here.

Above ~250 km the effect of collisions on ion bulk motion can be neglected. The frozen-in condition holds and the plasma moves according to $\mathbf{E} \times \mathbf{B}$ drift. At ~120 km the ion gyro frequency equals the ion-neutral collision frequency and the plasma motion is equally influenced by the $\mathbf{E} \times \mathbf{B}$ forcing and by collisions with the neutral gas, and below ~90 km the ion motion is fully collision-dominated so that that the ion gas motion is equal to the neutral gas motion.

However, even a very small collision frequency will have a measurable effect, by causing heating of the ion gas and the neutral gas. This can be approached in two ways: the Joule heating picture, where the ionosphere is a conductor with

a finite resistivity, and the current generates heat; or the ion-frictional picture, where ions in ordered $\mathbf{E} \times \mathbf{B}$ motion bump into neutrals and their motion becomes disordered, i.e. ordered kinetic energy becomes random thermal energy. The equivalence of these two approaches is demonstrated by Thayer and Semeter [2004], and which approach one chooses is generally based on what data you are working with—if you measure electric fields and currents directly you'd use the Joule heating approach, and if you measure bulk gas properites you'd use the kinetic approach.

2.3.1 Joule heating: Currents in the ionosphere

Currents in the ionosphere are usually separated into three components: A field-aligned current component $\mathbf{J}_\parallel$, the Pedersen current $\mathbf{J}_P$ which is in the direction of the component of the electric field orthogonal to the magnetic field ($\mathbf{J}_P \parallel \mathbf{E}_\perp$), and the Hall current $\mathbf{J}_H$, which is a polarization current orthogonal to $\mathbf{J}_\parallel$ and $\mathbf{J}_P$. Introducing the mobility coefficients $k_i = \Omega_i/\nu_{in}$ and $k_e = \Omega_i/\nu_{en}$ where Ω are the ion/electron gyrofrequencies, and writing e for the proton charge, the ionospheric condictivities corresponding to the three current components are

$$\sigma_P = \frac{n_e e}{B}\left(\frac{k_e}{1+k_e^2} + \frac{k_i}{1+k_i^2}\right) \tag{2.5}$$

$$\sigma_H = \frac{n_e e}{B}\left(\frac{k_e}{1+k_e^2} - \frac{k_i}{1+k_i^2}\right) \tag{2.6}$$

$$\sigma_\parallel = \frac{n_e e}{B}\left(k_e + k_i\right) \tag{2.7}$$

and the total current density is

$$\mathbf{j} = \sigma_P \mathbf{E}_\perp - \sigma_H \frac{\mathbf{E}\times\mathbf{B}}{B} + \sigma_\parallel \mathbf{E}_\parallel \tag{2.8}$$

The Pedersen current is strongest near the altitude where $\Omega_i = \nu_{in}$, i.e. $k_i = 1$. This is primarily determined by the neutral density and composition. The Hall current is strongest near the E region peak electron density. The Pedersen current is of interest because it converts electromagnetic energy to heat. The Hall current is orthogonal to the electric field and therefore non-dissipative, i.e. causes no ohmic heating: $\mathbf{j}_H \cdot \mathbf{E} = 0$.

There are additional currents due to diffusion and gravity, and the neutral wind modifies the current equations. For further reading, see Chapter 7 of Brekke

[1997].

2.3.2 Ion-frictional heating of the ion gas

Since there are ~1000 neutral molecules for each ion, the neutral atmosphere influences the motion of the ion gas far more than the motion of the ion gas affects the neutral wind. The ion motion is controlled by the $\mathbf{E} \times \mathbf{B}$ drift and ionospheric electric fields. There is some momentum transfer from the ion gas to the neutral gas, but only on longer timescales, order of 20 minutes to several hours in the dark polar ionosphere [Baron and Wand, 1983; Maeda *et al.*, 2009]. On scales of a few minutes the ion gas motion does not have a large effect on the neutral wind, and the two move essentially independently, with neutral velocity vector ($\mathbf{v}_n$) in one direction and the ion gas in another direction ($\mathbf{v}_i$).

For timescales longer than around ten seconds and below ~400 km, frictional heating of the ions is reasonably well described by the equation

$$T_i - T_n = \frac{m_n}{3k_B}(\mathbf{v}_i - \mathbf{v}_n)^2 \tag{2.9}$$

T_i is the ion temperature, T_n is the temperature of the neutral gas, m_n is the mean mass of a molecule of neutral gas, and k_B is Boltzmann's constant. $\mathbf{v_i}$ and $\mathbf{v}_n$ are ion and neutral velocity vectors. See paper 1 for further discussion of this equation, or St.-Maurice and Hanson [1982]. This simple relationship between ion flow speeds and temperatures allows us to use temperature enhancements as a proxy for reconnection-driven plasma flows. The neutral parameters are difficult to measure, so we often have to rely on models or long-term averages. Data from the CHAMP spacecraft show that the average neutral wind near the cusp is relatively slow, from stagnant to 200 m/s and directed poleward to westward [Bjoland *et al.*, 2015; Förster *et al.*, 2008].

2.3.3 Ion-frictional heating of the thermosphere

The neutral gas is heated by particle precipitation and by ion-fricitonal heating, similar to the ion gas. Thayer and Semeter [2004] give a review of different heating mechanisms. For ion-frictional heating they give the equation

$$\frac{\delta E_n}{\delta t} = \sum_i n_i m_i \nu_{in}(\mathbf{v}_i - \mathbf{v}_n)^2 \tag{2.10}$$

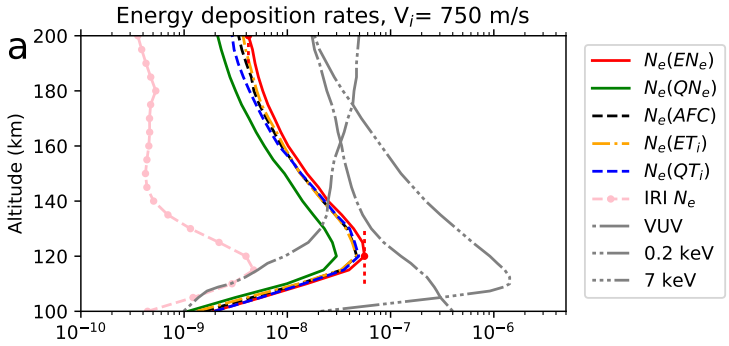

Figure 2.4: Electromagnetic energy deposition rates in the cusp computed from several model N_e profiles (colored lines) when the ion-neutral flow shear is 750 m/s, and UV and particle precipitation energy depositions (grey lines). The grey lines were taken from Thayer and Semeter [2004]. The solid color profiles are from ESR measurements; the dash-dotted color profile is the model in current common usage. From paper 3.

or, equivalently (using Equation 2.9),

$$\frac{\delta E_n}{\delta t} = \frac{3k_B}{m_n} \sum_i n_i m_i \nu_{in} (T_i - T_n) \tag{2.11}$$

$\delta E_n / \delta t$ is the energy deposition rate for one neutral species. n_i is the partial number density of the ion gas, m_i the mean molecular mass of the ion, and ν_{in} the ion-neutral collision frequency. The energy deposition rate is summed over all available ion species, and the total energy deposition rate is the sum of all the energy deposition rates into all neutral gas species.

In addition, particle precipitation and solar UV radiation will heat the thermosphere. High-energy electron precipitation as found on the nightside will do most of the heating at low altitudes (100–140 km) while the softer precipitation in the cusp will deposit most of the energy at higher altitudes (150–200 km).

Chapter 3

The Solar Wind-Earth system

3.1 The Earth's magnetic field

The Earth's magnetic field can be approximated as the field of a dipole, located inside the Earth, with a magnetic axis tilted 11.2° from the rotation axis of the Earth. If the source of the magnetic field was confined to the Earth's center, this would be a reasonably good approximation of the field near the surface. However, the Earth's field has many contributions from magnetic sources in the crust and mantle, and so the dipole model isn't adequate for scientific use. Furthermore, the Earth's magnetic field is slowly changing, so any model field must be updated regularly. The International Geomagnetic Reference Field (IGRF) model [Thébault *et al.*, 2015] is a detailed empirical model of the Earth's internal magnetic field. It is a spherical harmonic model updated every five years to account for the change over time of the magnetic field, and is suitable for ionospheric work. It does not take into account external sources (i.e. ionospheric, magnetospheric and solar wind/magnetopause currents), so it will not model the magnetosphere or reproduce storm-time disturbances.

3.2 The solar wind

The solar wind is a stream of hot charged particles continuously flowing from the Sun in all directions. It is a fully ionized plasma, consisting of protons, electrons, and some helium nuclei. The solar wind is supersonic, meaning that the solar wind is travelling away from the Sun faster than plasma waves can travel through the plasma towards the Sun.

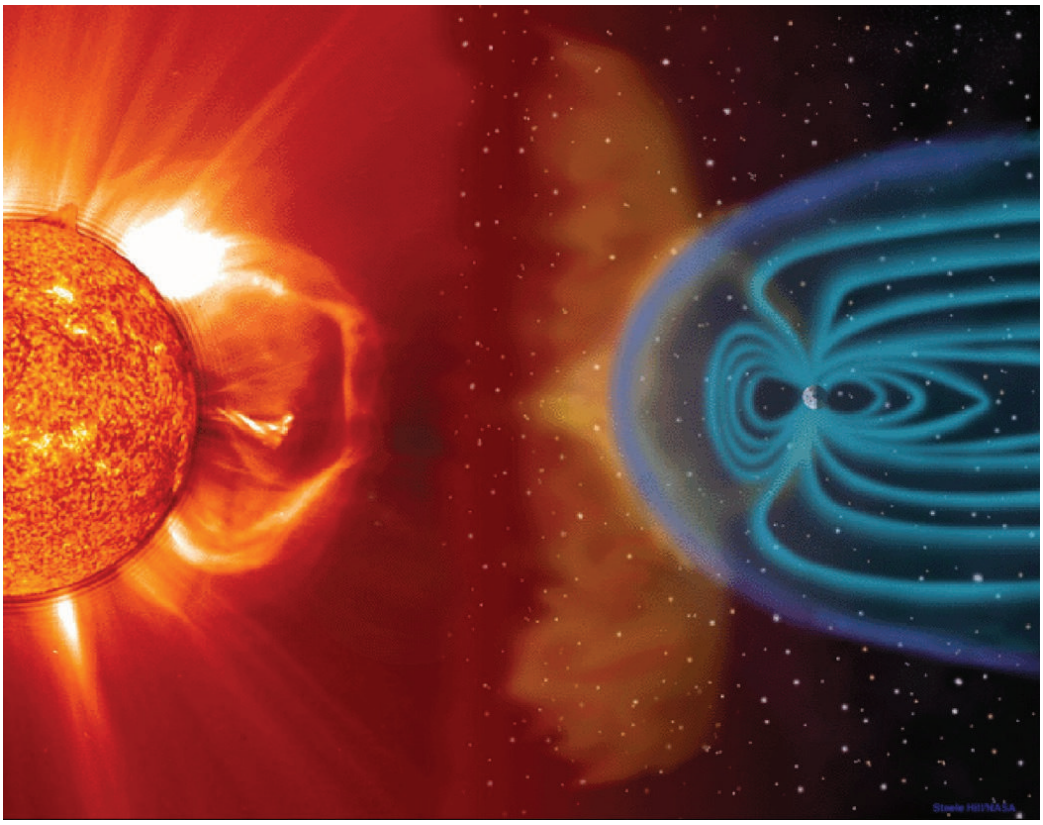

Figure 3.1: Illustration of the solar wind streaming off the Sun and shaping the Earth's magnetic field. The shape of the Sun's magnetic field can be seen in the shape of the solar wind structures coming off the sun. Credits: Magnetosphere: NASA, the Sun: ESA/NASA SOHO

The solar wind carries with it a frozen-in magnetic field, called the interplanetary magnetic field (IMF). This field changes in strength and direction depending on magnetic conditions when the wind was sent out from the Sun's chaotic atmosphere.

3.3 The magnetosphere

The solar wind is a superconducting fluid. When the solar wind meets the Earth, the magnetic fields of the Earth and the solar wind interact to deform the Earth's magnetic field, compressing it on the sunward side and stretching it into a long tail on the nightside. A magnetic boundary called the *magnetopause* is created. Boundary currents are induced in the magnetopause as the Earth's field is dis-

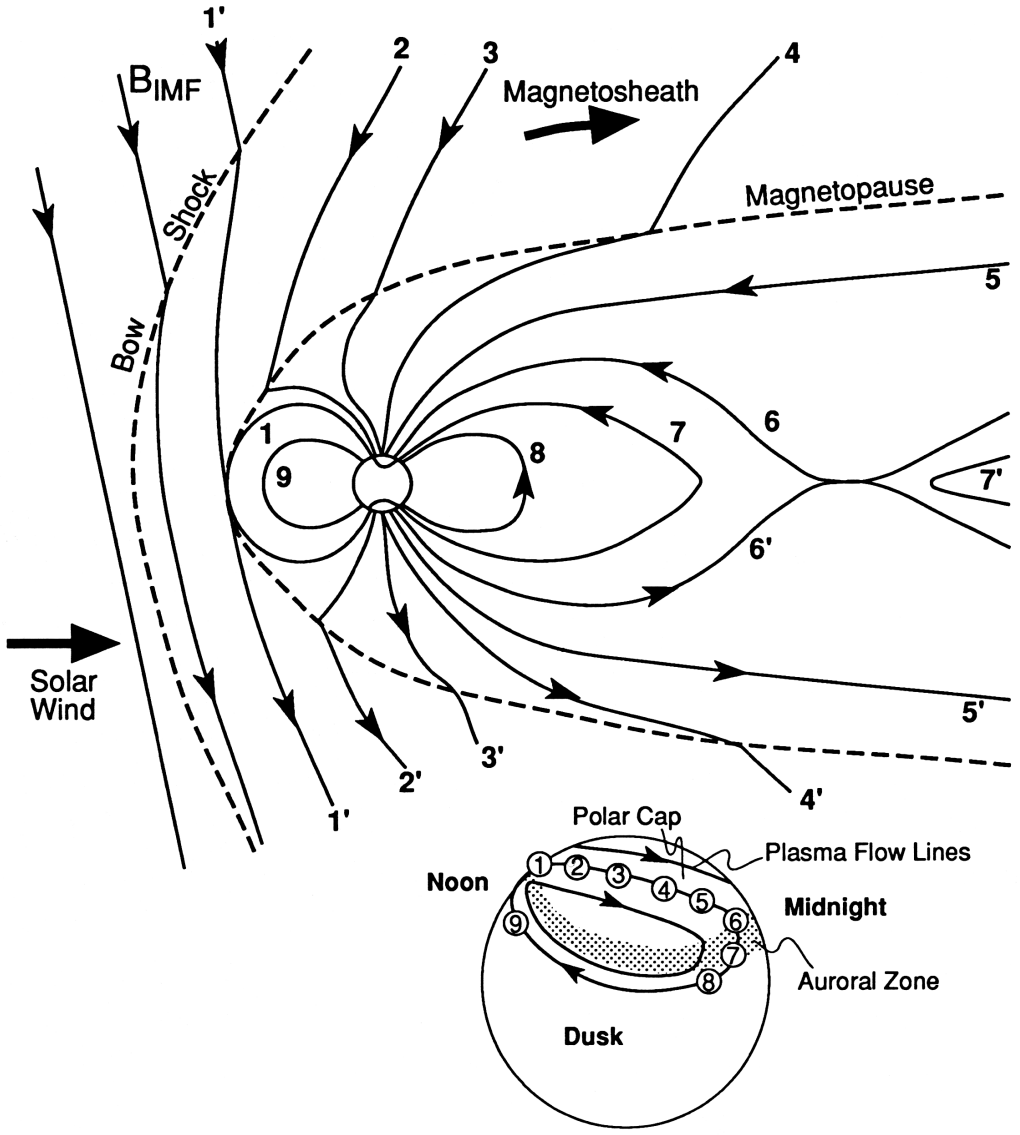

Figure 3.2: Sketch of magnetosphere cross-section, with reconnecting field lines. Almost all of the magnetosphere is magnetically connected to high latitudes on Earth. The solar wind is drawn directed southward ($B_Z < 0$). The solar wind field reconnects with the Earth fields, opening magnetic field lines in the magnetosphere. The reconnected field lines are dragged along with the solar wind and drape over the magnetosphere tail. Numbers indicate how field lines map down to the polar cap. From Hughes [1995].

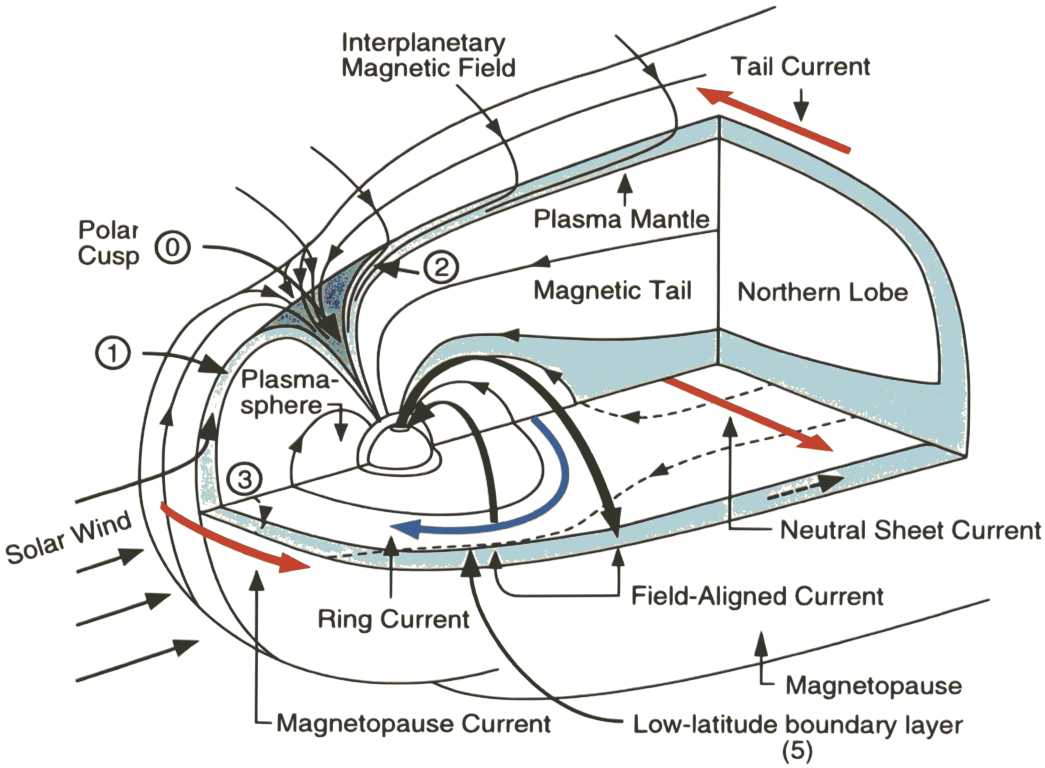

Figure 3.3: Anatomy of the magnetosphere, showing some of the regions and currents of the magnetosphere. Of importance to this thesis is the cusp (labeled 0). From Sandholt *et al.* [2002].

torted. The magnetopause can be pictured as a distorted bubble, within which is a region of space magnetically tied to the Earth, the *magnetosphere*. Outside is the solar wind, which is connected to the Sun.

Figure 3.2 shows conceptually the interaction of the solar wind with the Earth's magnetic field, and how the dipole-like Earth field is compressed in front and stretched into an elongated tail on the nightside. The tail extends for several hundred Earth radiuses outward, and probably doesn't have a sharp, well-defined end.

Figure 3.3 shows a conceptual sketch of the magnetosphere with important regions and currents marked. Of particular interest to this thesis are the cusps, which are the funnel-shaped structures where the magnetic field lines from all over the magnetopause (the magnetosphere surface) go down toward the Earth, and through the magnetosphere into the ionosphere. The cusps are the most direct paths of energy and plasma transfer between the solar wind and the iono-

sphere.

3.4 Magnetic reconnection

As the solar wind streams past the Earth the solar wind's magnetic field plasma properties will be seen to change, while the direction of the Earth's field stays the same. When the solar wind field has a component antiparallel to the Earth's field at the magnetopause, the fields will connect when they meet at the magnetopause. The frozen-in condition will break down locally when the magnetic field shear is very large, and plasma, momentum and energy can cross the magnetopause. Conceptually, we can think of this as both the solar wind field lines and the Earth-connected field lines breaking apart at the reconnection point, and the severed field lines re-attaching across the magnetopause.

The frozen-in approximation will quickly become valid again as solar wind field lines convect outward. The solar-wind end of the field lines follow the solar wind outward, pulling the Earth-attached end along, see Figure 3.2.

The newly reconnected flux tube will have a sharp kink immediately after reconnection, and this kink is rapidly straightened as the flux tube is pulled along with the solar wind. This accelerates the plasma on the field line in a process somewhat similar to a slingshot: plasma is accelerated away from the kink in both directions (points 1, 2, and 3 in Figure 3.2.)

Reconnection on the dayside maps down to the dayside on Earth. Reconnection also happens in the magnetospheric tail, across the mid-plane (points 6 and 7 in Figure 3.2), but here field lines are closed rather than opened. Plasma is ejected both towards the Earth and into the solar wind (points 7 and 7'). The process is the same as on the dayside, but auroral acceleration processes in the tail greatly increases the energy of the precipitating electrons, creating the bright night-time aurora.

Reconnection can often happen in bursts. Rather than a smooth and continuous transfer of plasma and energy, a volume of field lines, a *flux tube*, reconnects as a unit. The ionospheric signature will then also be pulsed [f.ex. Lockwood *et al.*, 1993b; Lockwood and Wild, 1993; Lorentzen *et al.*, 2007; Sandholt *et al.*, 1993], with the aurora brightening and fading for each pulse rather than a continuous glow.

As new flux tubes are opened at the dayside and draped across the magnetosphere (points 3, 4 and 5), the internal flux tubes in the magnetotail are squeezed together and the tail cross-plane reconnection rate increases. Because of the time

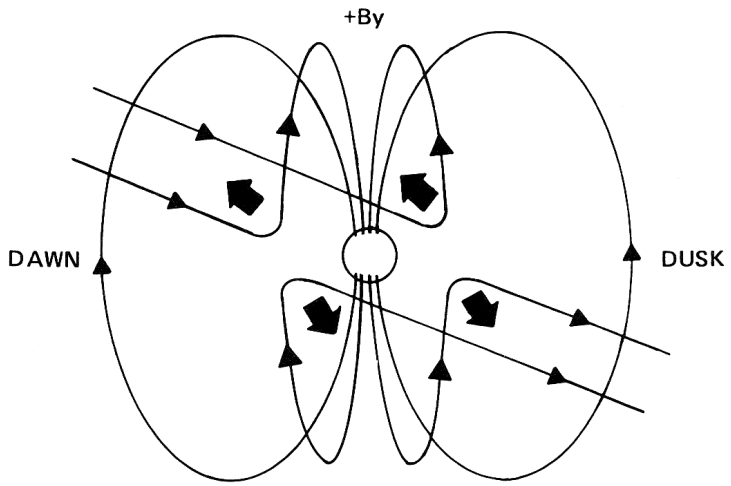

Figure 3.4: Illustration of reconnection seen from the Sun, when IMF $B_Y > 0$. The direction of relaxation of the flux-tube kink has a significant east-west component, which maps down to the ionosphere. From Kivelson [1995].

it takes to drape the flux tubes over the magnetotail, nightside reconnection happens a while after dayside reconnection. Studies by Hubert *et al.* [2006] and Milan [2004, 2013] suggest that onset of high reconnection rate on the dayside is followed by onset of high reconnection rate on the nightside with order of an hour delay.

3.5 Open and closed field lines

A field line with both ends going into the Earth is called a *closed* field line. A field line with one end on the Earth and one end in the solar wind is called an *open* field line. The field lines near the geomagnetic poles are all open. The part of the ionosphere that is on open field lines is known as the *polar cap*.

The aurora is primarily created by energy transferred on reconnected field lines from the magnetopause in the dayside or the midplane of the magnetotail on the nightside. This process places the auroral oval along the transition from open to closed field lines, called the *open-closed boundary*.

The cusp and the daytime auroral oval is on open field lines, while the nighttime auroral oval is on closed field lines. This is because the dayside aurora is created when field lines are opened on the magnetopause front, while the night aurora is created when field lines are closed in the magnetosphere tail.

If the IMF has a significant B_Y component, it will affect the polar cap flow. Figure 3.4 shows that when B_Y is strongly positive, the pull on the ionospheric footpoint will have a strong westward component in the northern hemisphere (eastward in the southern hemisphere). This will also create strong eastward or westward flow channels in the ionosphere. This is important when discussing ion-frictonal heating in Section 2.9.

Chapter 4

The thermosphere and the ionosphere

The ionosphere is the ionized component of the *thermosphere*, the upper part of the Earth's atmosphere. The thermosphere is weakly ionized, from ~100 to ~10 000 neutral molecules for each ion depending on altitude, ionospheric activity and solar activity. On lower latitudes the ionization is mainly due to solar X-rays and extreme UV radiation, but at high latitudes precipitation of particles from the magnetosphere and magnetopause/solar wind is also a significant contribution to ionization.

The composition of the neutral atmosphere changes significantly throughout the thermosphere. Below ~200 km molecular gases dominate, but at higher altitudes atomic gases begin to dominate.

Since the ions in the ionosphere are created from ionization of the neutral gas, the composition of the ion gas also changes with altitude. The lifetime of a free ion varies greatly: Below some 200 km it will recombine with a free electron in a matter of seconds, but above 400 km it may survive for hours.

The ionosphere is commonly divided into three regions/layers: D, E and F. The D region is the lowest, which lies between 60 and 90 km altitude. It only exists as a distinct structure in the ionoization profile at daytime, when solar radiation can produce ionization. Negative ions can exist in the D region because of the high neutral density. Figure 4.3 shows typical midlatitude profiles with the locations of the layers indicated.

Above the D region, from 90 up to 150 km altitude, lies the E region. This region is dominated by molecular positive ions. The E region is created primarily by solar X-ray and EUV radiation, and the solar ionization vanishes at nighttime.

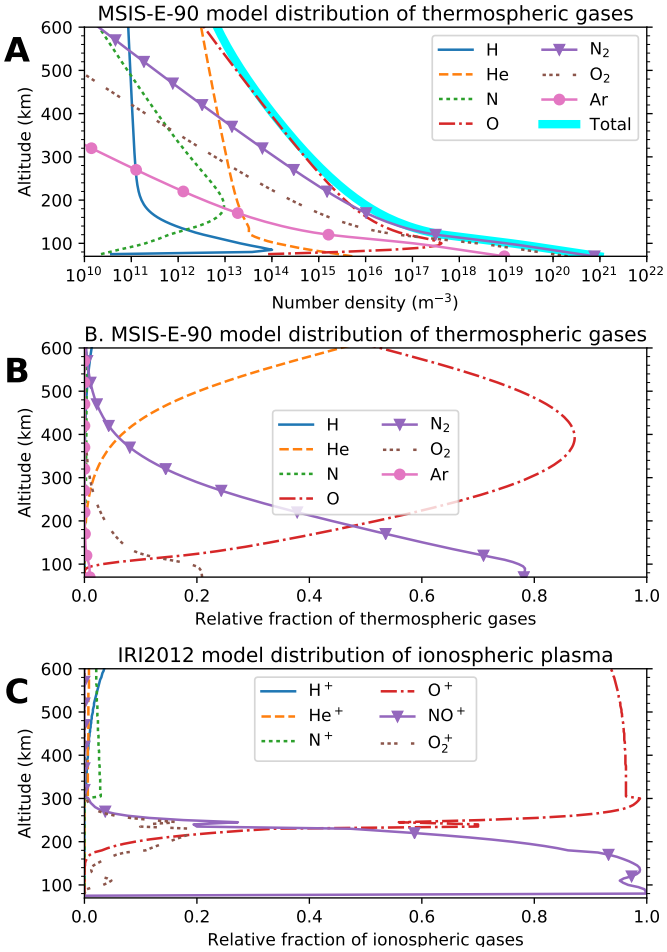

Figure 4.1: Model (A, B) thermospheric and (C) ionospheric constitutent gases between 70 and 1000 km altitude, using the MSIS-E-90 [Hedin, 1991] thermospheric model and IRI2012 [Bilitza *et al.*, 2014] ionospheric model. Curves shown are computed for 20 Dec 1998 at 08:50 UT (12 MLT) over the ESR site. **A** shows the number densities of the gases, with the thick blue line showing the total number density. **B** shows the fractional distribution of each thermospheric gas, using the same legend as **A**. Finally, **C** shows the fractional distribution of ionospheric ions.

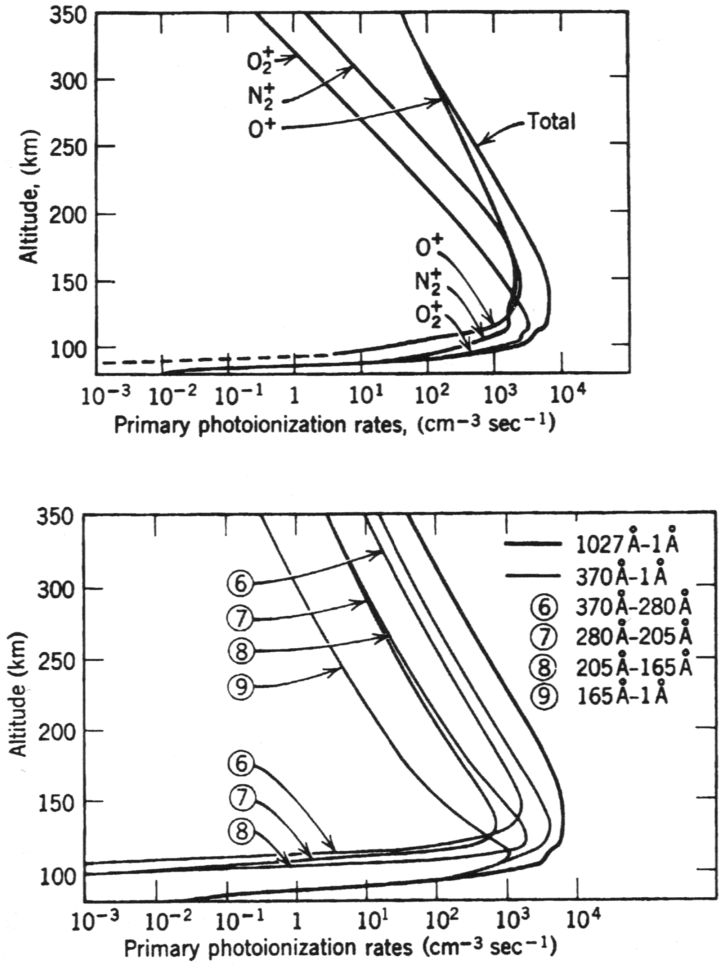

Figure 4.2: Calculated ionization rates in the E and F regions for summer midlatitude thermosphere. Top: Production rates of the three important ions. Bottom: Total ionization rates for different wavelengths of solar radiation. Wavelengths are given in Ångstrøms: 1 Å = 0.1 nm. The line marked 9 corresponds to X-rays, the other numbered lines to various parts of the ultraviolet spectrum. From Hinteregger *et al.* [1965]/Brekke [1997].

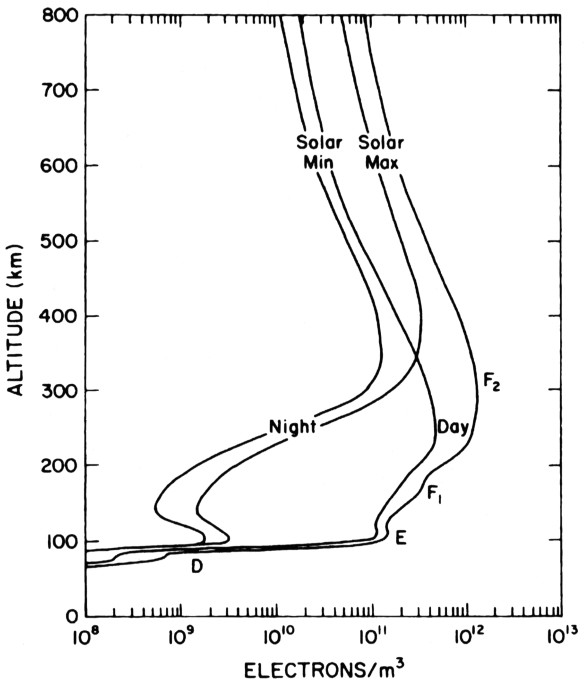

Figure 4.3: Example electron density profiles for the midlatitude ionosphere for day and night at solar maximum and minimum, showing the ionospheric region peaks. From Richmond [1987]/Brekke [1997].

However, precipitation of magnetospheric particles can also create ionization at this altitude at night.

Above the the E region lies the F region, from ~150 km altitude up to the top of the ionosphere. The F region is mainly composed of atomic ions. The peak ion density normally lies between 300–400 km altitude. At this altitude ions can survive for hours before recombining with free electrons, and transport of F region plasma from sunlit areas into the dark polar regions is an important mechanism for creating horizontal gradients in polar cap ion density [e.g. Crowley, 1996; Lockwood and Carlson, 1992; Semeter *et al.*, 2003].

Figure 4.1 shows model profiles of thermospheric partial gases, and the fractional distribution of the neutral [MSIS-E-90 model, Hedin, 1991] and ion gases [IRI2012 model, Bilitza *et al.*, 2014]. The models show the E region neutral gas dominated by N_2 with some O_2, and a transition to an O-dominated thermosphere. The dominant E region ion is NO^+, with some ${O_2}^+$ in the lower F region and the F region otherwise dominated by O^+. Above ~600 km altitude, helium and He^+ become dominant. Note that these are model results, and actual com-

position can vary significantly. For example, ionospheric heating can transiently make the F region up to ~350 km dominated by molecular ions [Lockwood *et al.*, 1993a].

The F region can sometimes during the daytime have a smaller peak below the main peak. When this happens these peaks are named F1 and F2, with F1 lower and F2 upper.

The ionospheric ions and thermospheric atomic gases are the result of a complex chain of ionization and recombination. The main ions produced directly by photoionization of thermospheric neutral gases below ~500 km are O_2^+, N_2^+ and O^+. The other ions as well as the atomic neutrals are formed in a complex chain of chemical reactions. Solar UV and X-ray radiation can, depending on wavelength, ionize atoms and molecules or directly dissociate molecules into neutral atoms [Brekke, 1997, p. 207]. Table 4.1 lists various chemical reactions that create or destroy ions. The reaction rates vary, see Brekke [1997] for more details. Reactions involving negative ions occur mainly in the D region. The number of reactions listed in the table hints at the complexity of ionospheric chemistry.

4.1 Ionospheric reference frames

Many phenomena in the ionosphere are strongly influenced by the geomagnetic field. For this reason it is useful to define coordinate systems based on the geomagnetic field.

4.1.1 Geomagnetic coordinates in the ionosphere

There are several magnetic coordinate systems used for ionosphere studies. I have used the Altitude Adjusted Corrected Geomagnetic coordinates (AACGM) [Baker and Wing, 1989; Shepherd, 2014]. It is similar to the older Corrected Geomagnetic coordinates (CGM) [f.ex. Gustafsson *et al.*, 1992], and for my purposes they are interchangeable.

AACGM defines geomagnetic coordinates by means of two magnetic field models: The IGRF model and a simple centered dipole model. Figure 4.4 illustrates the process. The AACGM coordinate is found by starting at some point at or above the Earth's surface, and following the IGRF model fieldline outwards until it meets the magnetic dipole equatorial plane. Then it traces back along the *dipole* field until it reaches the Earth's surface, and the geographic coordinates of this end point are the geomagnetic coordinates of the starting point. If the

Table 4.1: Ion production/loss reactions in the thermosphere

Photoionization	
$N_2 + h\nu$	$\longrightarrow {N_2}^+ + e$
$O_2 + h\nu$	$\longrightarrow {O_2}^+ + e$
$O + h\nu$	$\longrightarrow O^+ + e$
$He + h\nu$	$\longrightarrow He^+ + e$
Dissociative recombination	
$NO^+ + e$	$\longrightarrow N + O$
${O_2}^+ + e$	$\longrightarrow O + O$
${N_2}^+ + e$	$\longrightarrow N + N$
Rearrangement	
$O^+ + N_2$	$\longrightarrow NO^+ + N$
$O^+ + O_2$	$\longrightarrow {O_2}^+ + O$
${O_2}^+ + NO$	$\longrightarrow NO^+ + O_2$
${O_2}^+ + N_2$	$\longrightarrow NO^+ + NO$
${N_2}^+ + O$	$\longrightarrow NO^+ + NO$
${N_2}^+ + O_2$	$\longrightarrow N_2 + {O_2}^+$
Radiative recombination	
$O^+ + e$	$\longrightarrow O + h\nu$
Electron attachment	
$O_2 + M + e$	$\longrightarrow {O_2}^- + M$
$O + e$	$\longrightarrow O^- + h\nu$
Electron detachment	
${O_2}^- + h\nu$	$\longrightarrow O_2 + e$
${O_2}^- + N_2$	$\longrightarrow O_2 + N_2 + e$
${O_2}^- + O_2$	$\longrightarrow O_2 + O_2 + e$
$O - 2 + O$	$\longrightarrow O_3 + e$
$O^- + O$	$\longrightarrow O_2 + e$
Ion-ion recombination	
${O_2}^+ + {O_2}^-$	$\longrightarrow O_2 + O_2$
${O_2}^+ + {O_2}^- + M$	$\longrightarrow O_2 + O_2 + M$

Adapted from Brekke [1997]. M can be one of several molecules able to absorb excess energy from the reaction. Energetic photons are written as $h\nu$, and e are free electrons. Atoms and molecules will frequently be in an excited state (not shown) after the reaction.

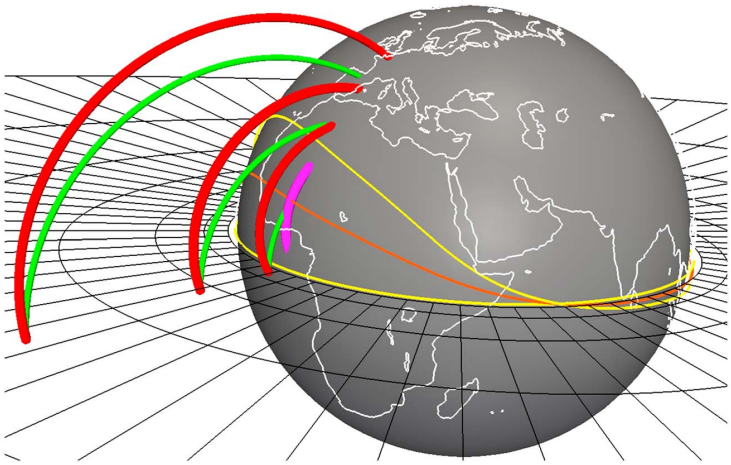

Figure 4.4: AACGM coordinate definition. Coordinates are found by following the red line outwards along the IGRF model field out to the dipole equatorial plane, and then back along the dipole field (green). AACGM is undefined between the two yellow lines. From Shepherd [2014].

outward trace encounters the Earth's surface before it reaches the dipole equatorial plane, AACGM is undefined at the origin point. Since the Earth's magnetic field is slowly changing, the AACGM coordinate of a point on the surface is also time-dependent.

Figure 4.5 shows what the AACGM coordinate system looks around the North Pole. Features of particular interest are: 1) it points to the geomagnetic pole, currently located on Ellesmere Island, Canada. 2) the coordinate system is deformed. This deformation is because the magnetic field is not perfectly centered inside the Earth.

4.1.2 Magnetic local time (MLT)

Once we have a magnetic coordinate system, we can define a magnetic local time. The principle is: A magnetic field line which crosses directly above the subsolar point (the point on the Earth's surface where the Sun is perfectly in zenith) is at 12 MLT, and 15° change in magnetic longitude corresponds to a change of 1 hour MLT.

In practice there are complications, caused amongst other things by AACGM not being defined everywhere. Different MLT calculators may well give different results depending on the underlying algorithms.

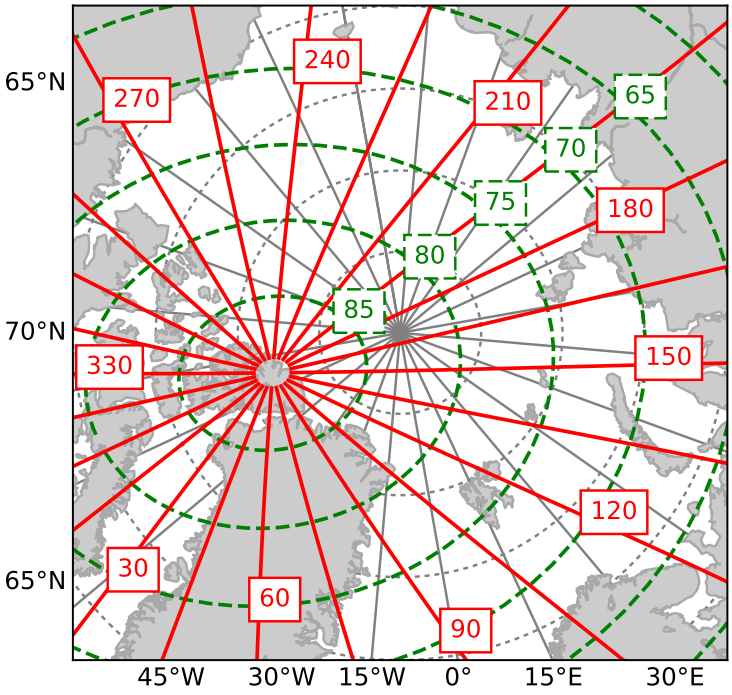

Figure 4.5: Geographic (grey) and AACGM coordinate grid (red magnetic longitude MLON, green magnetic latitude MLAT) around the North Pole. Solid longitude lines mark centers of time zones (15° wide), dashed lines mark edges. Magnetic local time (MLT) is constant along lines of constant MLON. The AACGM grid is computed for 250 km altitude and epoch 2017.

MLT is often used as a Sun-aligned east-west coordinate, instead of magnetic longitude which is fixed to the rotating Earth. Since the Earth's magnetosphere is day-night-oriented due to its interaction with the solar wind, the mapping of the magnetopause to the ionosphere is also day-night-oriented.

In Longyearbyen, 12:00 MLT was around 08:50 UT around year 2000, and is now (2017) around 09:10 UT according to the CGM calculator at `http://omniweb.gsfc.nasa.gov/vitmo/cgm_vitmo.html`. It's worth noting that the AACGM calculator at `http://sdnet.thayer.dartmouth.edu/aacgm/aacgm_calc.php#AACGM` gives 09:30 UT as the time of magnetic noon in Longyearbyen (2017). Implementation issues aside, the MLT of a point on the Earth at a given UT will have an annual oscillation (order of 5–10 minutes) due to the seasonal north-south motion of the subsolar point, as well as a slow drift due to the gradual change of the Earth's magnetic field.

4.2 The ionospheric cusp

The ionospheric cusp is the part of the ionosphere where the magnetospheric cusp field lines map down to the ionosphere. The north-south location of the cusp varies. The rotation of the Earth will in theory bring Svalbard underneath the cusp every day, but it might be far to the north of the instruments in Longyearbyen, or it could be right overhead, or a bit to the south. This is controlled by the balance of reconnection on the dayside and nightside, and by how much the solar wind compresses the magnetosphere front [Cowley and Lockwood, 1992; Sandholt *et al.*, 1994; Southwood, 1987]. Reconnection on the dayside opens flux tubes and adds open flux to the polar cap, pushing the cusp a little equatorward, while reconnection on the nightside, in the midplane of the magnetosphere tail, will close flux tubes and remove flux from the polar caps, pulling the cusp toward the pole. The day and night reconnection rates are balanced in the long term, but not on a minute-by-minute timescale, so the cusp can move quite a lot north-south while it's overhead (the day studied in paper 1 and paper 2 is a good example of this). As nice as drawings such as Figure 3.2 (page 21) are to look at, we can't actually see the field lines from the ground, and unfortunately we don't have the thousands of satellites that would be needed to map the magnetosphere instantaneously and continuously. For this reason it's necessary to identify secondary signatures of when the cusp is overhead. Sometimes a satellite with a plasma spectrometer will pass overhead and measure the incoming particles directly, but most of the time we have to rely on what can be measured from the ground.

4.3 Ionospheric effects of dayside magnetopause reconnection

Reconnection sets up currents parallel to the magnetic field, known as field-aligned currents (FACs) or alternatively Birkeland currents, after the scientist Kristian Birkeland, who first suggested the existence of such currents. Electrons are the primary current carriers, and the ionospheric signature of an outgoing Birkeland current is the aurora, created by electrons accelerated along the field lines, colliding with and exciting neutral atoms in the ionosphere. Large horizontal current systems arise in the ionosphere, closing the circuit between incoming and outgoing Birkeland currents. The horizontal currents dissipate reconnection

energy as heat the ion and neutral gases, and the plasma in and around the polar cap is set in motion.

4.4 Precipitation-driven ionization

The plasma on newly reconnected field lines will rain down into the ionosphere. The light electrons arrive first, and their energy determine how deep into the ionosphere they penetrate. Electrons precipitating in the cusp have relatively low kinetic energy (~0.2 keV) compared to nightside electrons (5–20 keV) [Brekke, 1997; Newell and Meng, 1992; Newell *et al.*, 2004]. The precipitating electrons heat the electron gas and ionize neutral atoms and molecules. A sudden increase in ionization can be observed above ~150 km [f.ex. Carlson *et al.*, 2012].

4.5 The auroral oval

The auroral ovals are centered around the geomagnetic poles. The pole in the northern hemisphere lies in northern Canada, so the oval is skewed to the north in Europe and to the south in North America. The oval is wider on the nightside than on the dayside, and it is always oriented toward the sun as the Earth rotates under it. On the dayside the oval passes over Svalbard, or more correctly Svalbard passes under the oval. Figure 4.7 shows an example of a model of the dayside auroral oval [Sigernes *et al.*, –0022–2011] crossing directly over Svalbard during midwinter, when it is dark in the daytime on Svalbard.

This happy coincidence that the dayside portion of the auroral oval passes over Svalbard is a great boon to auroral science. Longyearbyen, at 78° north, is far enough north that there is hardly any twilight at noon around midwinter, and so the faint dayside aurora can be observed from the ground. The other locations far enough north for optical observations of dayside aurora require organizing a scientific expedition, while Longyearbyen is a fairly ordinary town with good infrastructure and easy access with regular mainland flights. Other locations where the dayside aurora passes overhead and civil infrastructure is in place are too far south. All of this makes Svalbard a hotspot of polar ionosphere research.

Figure 4.6: Red and green aurora over Svalbard. EISCAT Svalbard Radar facility in the foreground. Photo: Njål Gulbrandsen.

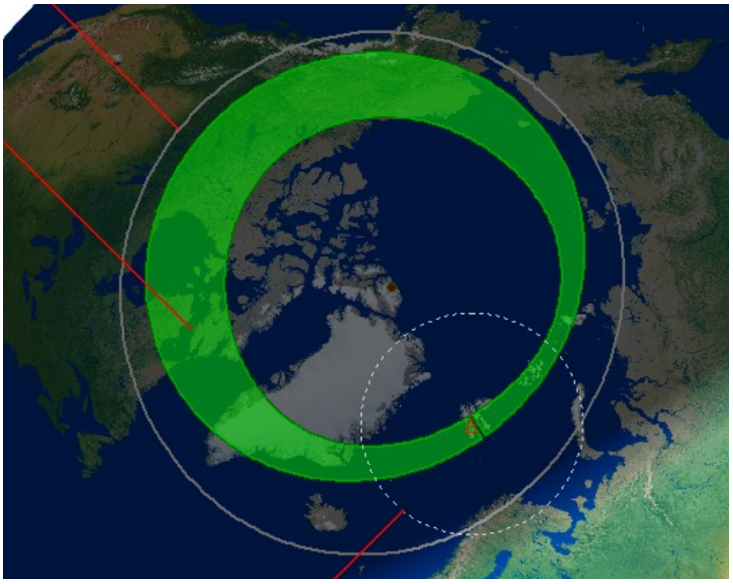

Figure 4.7: Illustration of the auroral oval over Svalbard on the dayside (SvalTrackII visualization). From Sigernes *et al.* [–0022–2011].

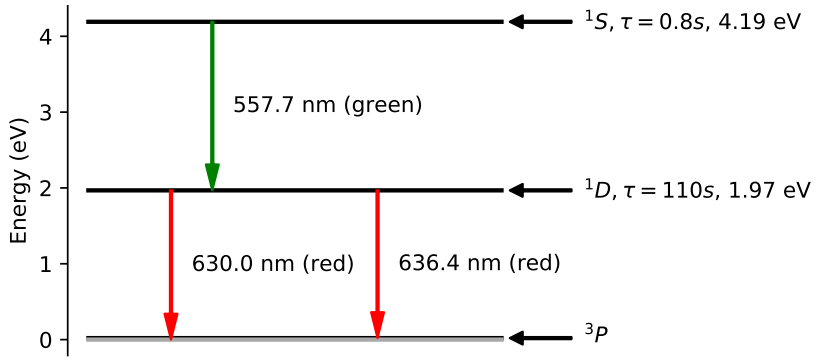

Figure 4.8: Atomic oxygen excitation states producing red and green emissions

4.6 Auroral excitation, quenching and emission

The aurora can contain light of many different colours. The most prominent ones are red and green, from atomic oxygen, and blue, from ionized molecular nitrogen. The blue aurora occurs on the lower edge of strong aurora, around 100 km. The green, from 100–150 km, is usually the most visible to the naked eye, and the red, normally 150–300 km, is faint at night. I will focus on the red and green lines here.

Precipitating electrons will cause both ionization and excitation of neutrals. An oxygen atom that's struck by an electron may be excited into a higher energy state. I will focus on the states named O(^{1}D) and O(^{1}S) in spectroscopic notation. The ground state is named O(^{3}P). Figure 4.8 show the relevant energy levels and the light emitted from electrons leaping down one level. As the figure shows, an excited atom in the ^{1}S may decay to the ^{1}D state, emitting a green photon of 557.7 nm wavelength. It may also decay directly to the ground state ^{3}P, emitting a photon of 297.2 nm ultraviolet (UVB) light, but this UV auroral light will be absorbed by the lower atmosphere and not reach the ground. It will however be detectable from space.

An atom in the ^{1}D state can then decay to the ground state ^{3}P. Because of fine structure in the ground state the atom may emit one of two slightly different wavelenghts, 630.0 nm or 636.4 nm (called the "red doublet"). The 636.4 nm transition has the lower transition probability of the two, and its light is about 1/3 as intense in the aurora as the 630.0 nm emission [Vallance Jones, 1974; Kvifte and

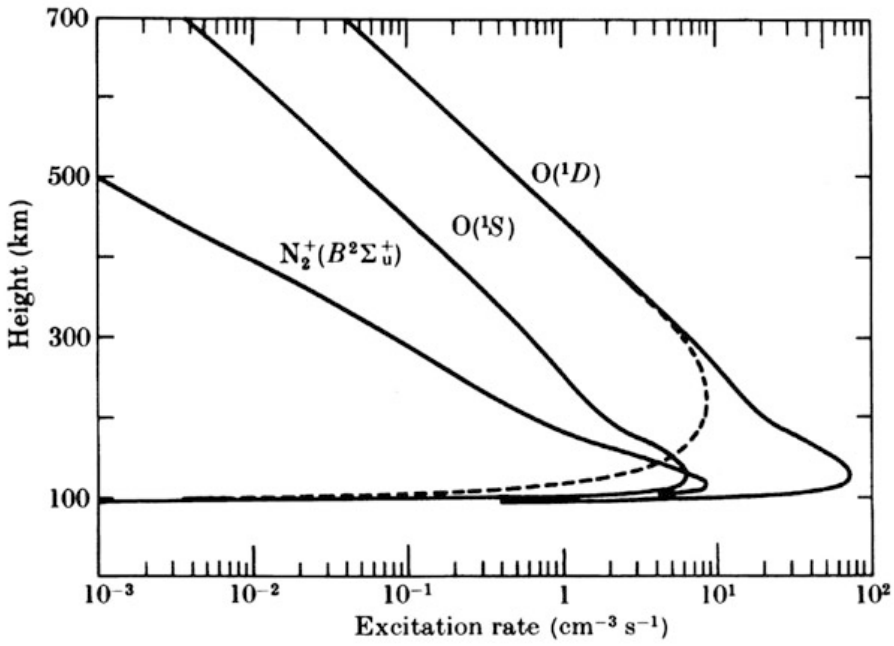

Figure 4.9: Model profiles of production of three metastable auroral excitation states for a given particle influx. The dashed line shows the effect of quenching of the red emissions. The blue $N_2{}^+$ line has a narrow peak just below the broader green emission. From Kamiyama [1966]/Brekke [1997], see Figure 9.26 of Brekke [1997] (or Figure 7.26 of Brekke [2013]) for details.

Vegard, 1947].

An oxygen atom in the ground state is most likely to be excited into the O(^{1}D) or O(^{1}S) states by collision with an electron with kinetic energy around 10–20 eV. The precipitating electrons initially have energies than this (~200 eV in the cusp aurora, 5–20 keV in the nightside aurora), but gradually lose that energy in collisions on their way down.

An important property of the ^{1}D and ^{1}S states is that they are so-called "metastable" states. A different way of describing this is that the transitions $^1\text{S} \longrightarrow {}^1\text{D}$ and $^1\text{D} \longrightarrow {}^3\text{P}$ are "forbidden" transitions. Most excited atomic states will decay spontaneously and emit a photon in a matter of microseconds or nanoseconds, but the metastable states have much longer lifetimes, for quantum-mechanical reasons which I will not go into here. The average lifetime for the ^{1}D state (red emissions) is 110 seconds, and for the ^{1}S state (green and UV emissions) 0.75 seconds. If the excited atom collides with another atom or molecule, the excitation energy will be converted to kinetic energy, and the atom will go to a lower-energy state without emitting a photon. This collision-driven conversion of excitation energy to gas internal energy (heat) is called *quenching*.

Figure 4.9 shows profiles of excitation for three states: the two oxygen states, and an $N_2{}^+$ excited state that produces a blue emission. The oxygen excitation rate profiles for the two states (middle and right solid lines) are very similar in shape but differ by about an order of magnitude. The dashed line shows how quenching limits the emission of the red auroral lines at lower altitudes to less than the green line. The green line, with its much shorter lifetime, is mostly quenched below 115 km.

The blue $N_2{}^+$ emission shown in Figure 4.9 has a narrow peak slightly below the O(^{1}S) peak. In strong night-time aurora it shows up as a blue lower edge to the auroral curtains.

Quenching causes the altitude separation of red and green aurora. If quenching did not occur, the emission rates would be equal to excitation rates and would follow the solid curves in Figure 4.9, and the red emission would dominate everywhere.

4.7 Cusp aurora

So why is the dayside/cusp aurora so much redder than the nightside aurora? The answer to this question lies in the energy of the precipitating electrons. The energetic nightside electrons penetrate down to 100–150 km altitude losing very

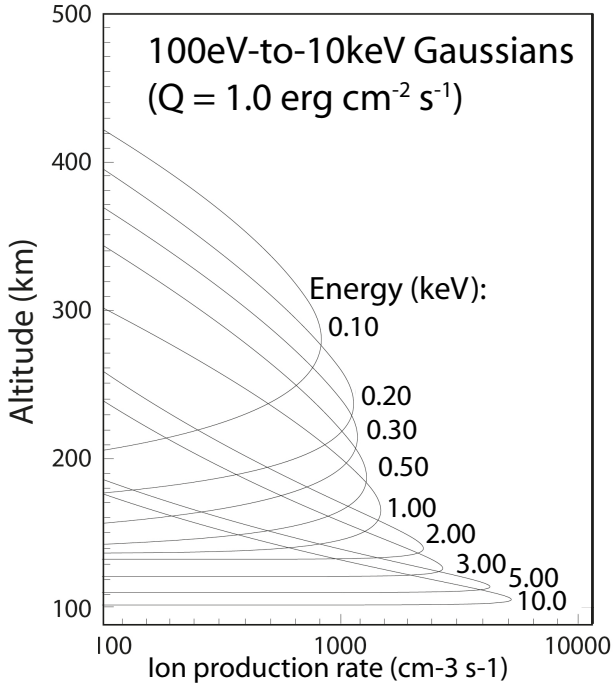

Figure 4.10: Ionization rates by altitude for model electron beams with a Gaussian energy distribution and various mean particle energies. Q is the beam energy flux (1 erg = 10^{-7} J), which is the same for all the modelled electron beams. From Carlson *et al.* [2012], see also Chapter 3 in Sandholt *et al.* [2002].

little energy to collisions on the way down, and deposit almost all their energy between 90–150 km altitude. The low-energy electrons in the cusp, on the other hand, lose their energy much more gradually, and deposit their energy mostly above 150 km where the red line emission is not quenched, and its excited state ^{1}D is more frequently excited than the green-emission state ^{1}S (see Figure 4.9). Figure 4.10 shows how electrons of different initial energies deposit their energy into the ionosphere through ionization: low-energy electrons ionize at higher altiudes over a large altitude range, and higher-energy electrons penetrate deeper and deposit their energy in a narrow energy range. Each electron has enough energy to cause many ionizations, and will lose some of that energy with each interaction. The same electrons will then cause excitation when their energies are suitably low (10–20 eV).

Figure 4.11 shows a similar calculation from the perspective of the remaining electron energy: incoming electrons lose energy with altitude for 1, 10 and

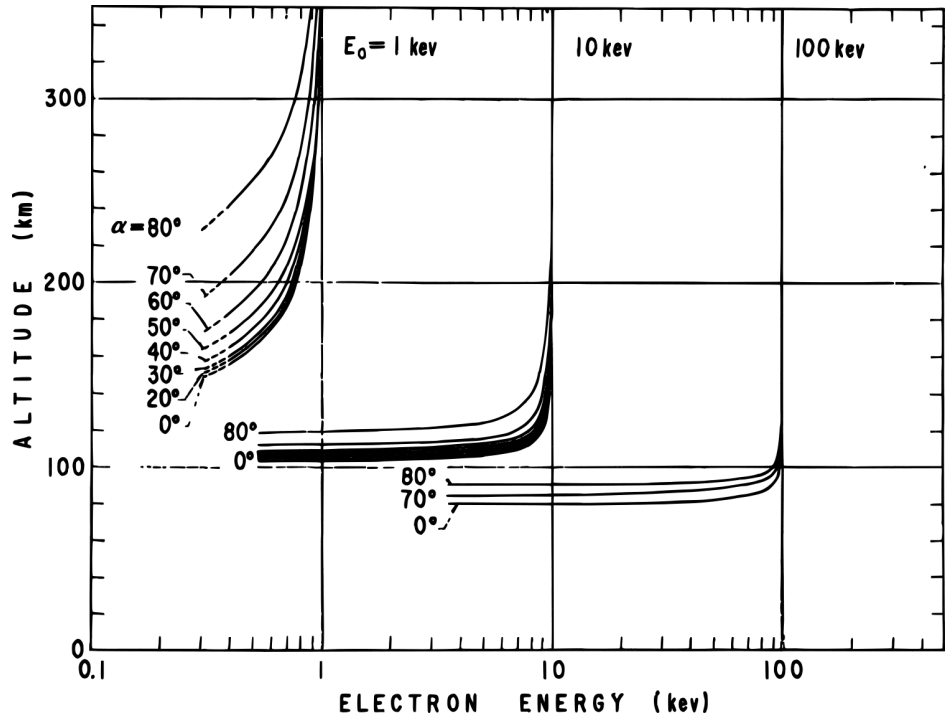

Figure 4.11: Figure showing how precipitating electrons lose their energy when coming down, for various initial energies and pitch angles. Low-energy electrons lose their energy gradually between 150–300 km, while energetic electrons "hit a wall" around 100–125 km. From Kamiyama [1967].

100 keV electrons and various pitch angles (angle between the electron velocity vector and magnetic field). Although energies below 100 eV are not shown, we can easily infer that the altitude range where precipitating electrons with initial energy 200 eV are reduced to 10–20 eV where excitation is likely is much larger (and higher up) than the similar excitation altitude range for 10 keV nightside precipitating electrons.

The auroral spectrum contains many spectral lines and bands, and the processes that create it are complex. I have only scratched the surface here. Interested readers may want to consult the textbooks suggested in the introduction, particularly Chapter 8 of Schunk and Nagy [2009]; some classic works on the subject are Chamberlain [1961] and Vallance Jones [1974].

4.8 Polar cap convection

The polar cap is the area within the auroral oval. The polar cap is entirely on open field lines, i.e. the magnetic field lines extend into the solar wind rather than looping back to the Earth and closing on themselves. When flux tubes are opened by dayside reconnection, the solar wind continues to blow past the Earth, carrying the solar wind portion of the flux tube along. This motion maps down to the ionosphere. The flux tubes stretch and drape over the magnetotail. As new flux tubes open on the dayside magnetopause and are transported towards the nightside by the solar wind, the open flux tubes pile up in the magnetotail.

As flux tubes are piled on top of the tail, the innermost tubes in the tail reconnect again to close flux. These newly closed flux tubes can then move around the Earth to the dayside. This process drives the large-scale convection of plasma in the polar cap. A very simple sketch of the process is shown in Figure 3.2 on page 21. The field lines numbered 1–9 show the progress of this dance. The numbered field lines map down to the corresponding place in the polar cap, shown on the globe on the bottom of the figure. Their footpoints move across the polar cap in a two-cell pattern.

The principles of ionospheric convection in the polar cap were descibed by Cowley and Lockwood [1992]. We can condense their description to three basic ideas: (1) magnetic flux density is constant, (2) only reconnection can add or remove magnetic flux from the polar cap, and (3) the polar cap tries to minimize its circumference.

Constant magnetic flux density means that the are of the polar cap is proportional to the amount of open flux inside it. The frozen-in approximation holds, so plasma moves along with the flux. We can then model the polar cap as the flow of an incompressible fluid. The process is shown in Figure 4.12. Row A shows addition of flux to the polar cap. First shown is the initial polar cap, flux area F, with magnetic local time (MLT) indicated. Additional flux dF is added, and the area of the polar cap increases. The dashed line indicates a circle of equivalent area. The plasma in the polar cap is set in motion in order to minimize the circumference, and a larger circle of area F+dF results. Row B shows the reverse process, removal of flux by nightside reconnection.

In practice the polar cap never has time to fully relax after reconnection before the next disturbance occurs. There will be flux added on the dayside and removed on the nightside, and the convection will be churning all the time. Row C shows the combination of the dayside and nightside forcing, resulting in a

two-cell convection pattern.

The actual polar cap flow is of course more complex than this, in particular it is strongly influenced by the strength and direction of the interplanetary magnetic field. In the long term the dayside and nightside reconnection rates (amount of flux added/removed per second) are equal, but on shorter timescales (minutes to an hour) reconnection rates will frequently be unbalanced. This manifests as the polar cap changing size on the same timescale, and one manifestation of this will be that the aurora moves equatorward or poleward as flux is added or removed (e.g. paper 1). See for example Cowley and Lockwood [1992], Moen *et al.* [1995], and Moen *et al.* [2004b]; and Cousins and Shepherd [2010], Greenwald *et al.* [1995], and Provan *et al.* [2002] for real-time radar mapping of the polar cap flow.

4.9 Motion of a reconnected flux tube footpoint

That's the global picture covered. Let us look at the reconnection of a single flux tube. Figure 4.13 shows the Southwood [1987] model of a recently reconnected flux tube, also known as a Flux Transfer Event (FTE). The thick black line is the border of the flux tube. The thin black lines show plasma flow inside and around the flux tube, dashed lines show horizontal Pedersen currents. Vertical lines show incoming (solid) and outgoing (dashed) Birkeland currents, with an auroral form on the outgoing current. The Pedersen currents close the current loop.

In addition to the aurora, the reconnection Birkeland currents sets the ionospheric plasma moving: an electric field between the two currents sets up an $\mathbf{E} \times \mathbf{B}$ drift. The flux tube footpoint is pulled through the ionosphere along the central streamline, and the ionospheric plasma outside the flux tube is pushed aside and flows around it. The plasma is frozen-in, so no plasma crosses the thick oval. The footpoint can be moving at speeds up to 3000 m/s shortly after reconnection, though 500–2000 m/s is more common. Outside the thick oval is a slower and less distinct return flow.

As the flux tube is pulled toward the nightside by the solar wind, the footpoint and the aurora is pulled toward the pole and into the polar cap. The aurora will fade after 5–10 minutes, and the convection around the footpoint will become indistinct after 10–20 minutes [Oksavik *et al.*, 2004, 2005; Rinne *et al.*, 2007]. The flux tube will gradually lose its identity as a distinct flux tube as it becomes identical to other spent flux tubes moving through the polar cap.

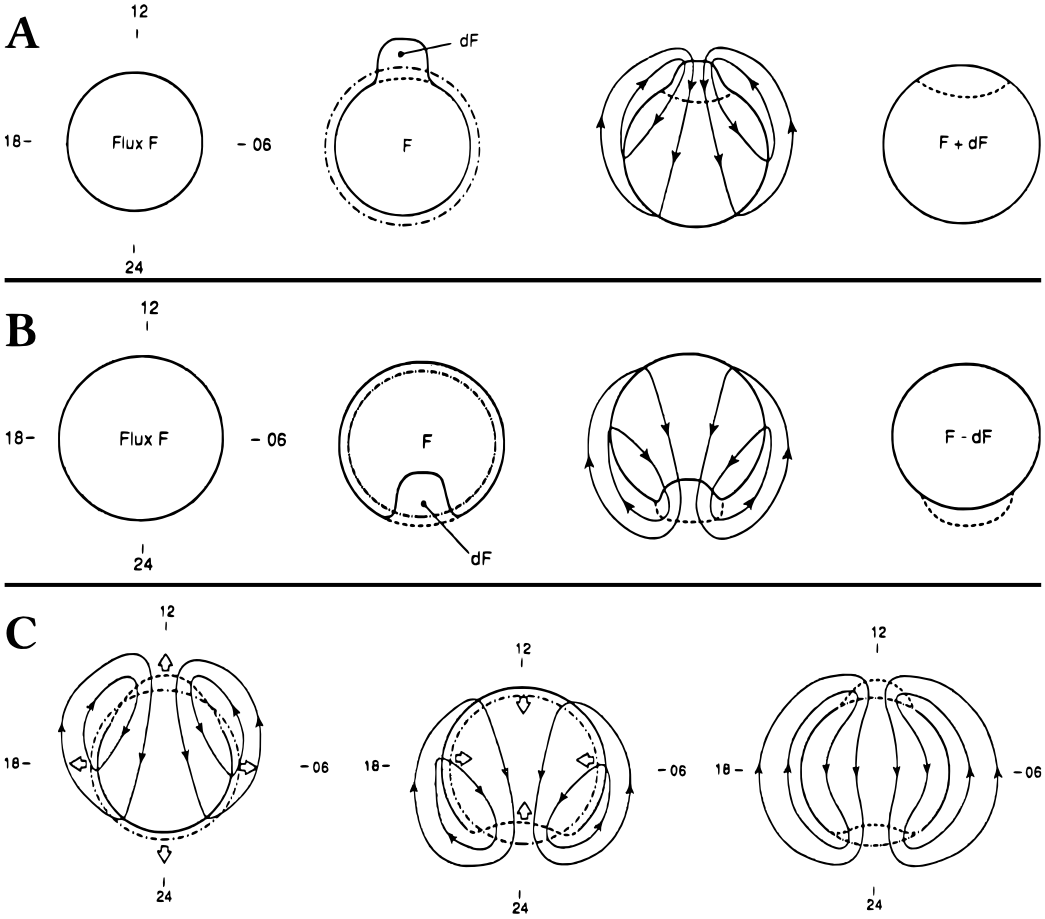

Figure 4.12: Schematic of reconnection-driven polar cap plasma flow. Solid black line is the open/closed boundary (OCB), closed loops with arrows are plasma streamlines. Note that no plasma crosses the OCB except at reconnection. **A**: Dayside reconnection adds flux tubes and plasma to the polar cap. **B**: Nightside reconnection removes flux from the polar cap. **C**: Left, middle: The individual contribution to the large-scale polar cap flow of dayside and nightside reconnection and how the flow circularizes the polar cap, and the combined effect. Adapted from Cowley and Lockwood [1992].

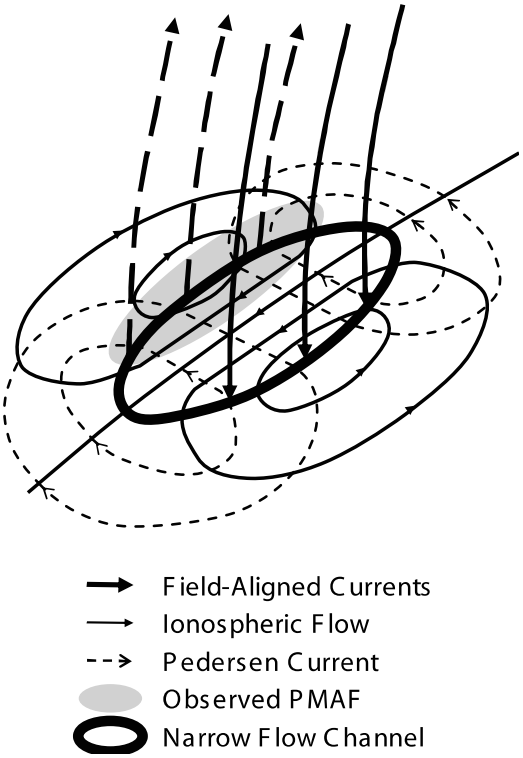

Figure 4.13: The Southwood [1987] model of an ionospheric footpoint of a recently reconnected flux tube. The footpoint convects along the centerline. No plasma crosses the thick oval. The convection along the streamlines may cause significant ion-frictional heating. From Oksavik *et al.* [2004].

From the ground, the aurora will be seen to be moving rapidly poleward. Auroral arcs moving in this way are called Poleward Moving Auroral Forms (PMAFs) [Moen *et al.*, 2008; Sandholt *et al.*, 1986, 1989, 1990; Sandholt and Lockwood, 1990; Sandholt *et al.*, 1998], and are a key optical signature of dayside reconnection and the ionospheric cusp.

In the event that IMF B_Y is strongly positive or negative, the motion of the flux tube will have a strong eastward or westward component the first few minutes after reconnection[Moen *et al.*, 1999; Rinne *et al.*, 2010]. This may increase the initial speed of the flux tube footpoint.

Studies of cusp flow channels by the EISCAT Svalbard Radar [f.ex. Oksavik *et al.*, 2004, 2005; Rinne *et al.*, 2007, 2010] show that cusp flow channels can be long, at least 1000 km, and narrow, 50–200 km. The flow patterns of observed events aren't isolated, but are affected by previous events and by the large-scale struc-

tures of the polar cap flow. Frequently only one flow vortex could be observed [Rinne *et al.*, 2007, 2011].

4.10 Ion upflow

The ionospheric plasma can often be observed to be moving up along the magnetic field. By *upflow* (or "thermal upflow") we mean bulk motion upwards of all the plasma in the measurement volume without significant distortion of the random (thermal) distribution of motion of the molecules. Upflow occurs primarily in the auroral zone, both on the dayside and nightside.

Ion upflows are sorted into two categories, Type 1 and Type 2 [Wahlund *et al.*, 1992]. Type 1 are driven primarily by heating of the ion gas, while Type 2 are driven by electron gas heating. The two types are discussed in detail in paper 1. They can be summmarized as follows:

When the ion gas is heated, it expands, like any other gas. Because the plasma is frozen-in, it can only expand along the magnetic field. This causes the ions to flow upward, in a Type 1 upflow.

When the electron gas is heated by precipitation, it expands, leaving the ions behind. This charge separation creates an *ambipolar* electric field that holds the electrons back and drag the ions along, in a Type 2 upflow.

4.11 Ion outflow and the ion fountain

The term *outflow* refers to ions on the topside of the ionosphere, moving at escape velocity or faster. H^+ in the upper ionosphere can become outflow at thermal speeds, but heavier ions require some additional energy source. The magnetosphere contains a significant amount of O^+ ions, which can only come from the ionosphere. Yau and André [1997] describe various types of outflowing ions that have been observed above the ionosphere. Unlike the bulk upflows found lower down, where all of the plasma is moving, only some fraction of the ions are accelerated into upflows. Probably the ions with the largest thermal random velocity interact with topside waves and precipitating particles to become accelerated and escape the atmosphere. The loss rate varies with solar activity. The maximum outflow measured by the DE-1 spacecraft, integrated over both polar caps, amounts to around 3×10^{26} ions/second, or around 8 kg of oxygen per second [Yau and André, 1997].

Several energization mechanisms have been proposed and studied. Broad-Band Extremely Low Frequency (BBELF) waves refer to low frequency electric field fluctuations. The frequency range is not precisely defined, and different papers may use from 100 Hz to several kHz as an upper limit [f.ex. Burchill *et al.*, 2004; Jacobsen and Moen, 2010; Kintner *et al.*, 2000].

The ion fountain is a phenomenon in the cusp/cleft area where ionospheric ions are heated, increasing in speed, and are then driven upward by the $\nabla \cdot B$ drift (magnetic bottling effect). Meanwhile, the plasma is convecting into the polar cap, and plasma upflow shuts off. The colder ions that were previously lifted fall back down, while the most energetic ions are able to continue rising and move into the magnetosphere. This is the "cusp/cleft ion fountain", a process where a fairly small area (the cusp/cleft) is the source of much of the O^+ ion outflow [Lockwood *et al.*, 1985a,b; Yau and André, 1997].

4.12 Neutral upwelling in the cusp

The thermosphere in the cusp is heated by ion-frictional heating, and expands upwards. This expanding "bubble" or "bulge" of rising gas will then have higher density than cold thermosphere at the same altitude. Unlike plasma which is constrained by the magnetic field, the heated gas can expand sideways, "spilling over" as it rises. This limits the altitude to which it can rise [Carlson *et al.*, 2012].

The CHAMP spacecraft found an unexpectedly strong and consistent increase in the cusp neutral density at around 400 km altitude [Lühr *et al.*, 2004; Lühr and Marker, 2013], up to a doubling of the thermospheric density. This thermospheric bulge was colocated with intense small-scale field-aligned currents, suggesting a link between dayside reconnection and the neutral density increase. This localized density increase is unique to the cusp.

Chapter 5

Data sources

This chapter briefly describes the different instruments and models used for this thesis.

5.1 EISCAT Svalbard Radar

The EISCAT Svalbard Radar (ESR) located outside Longyearbyen is one of several *inchoherent scatter* radars operated by the European Incoherent SCATter (EISCAT) organization. The other facilities are located in northern Norway, Sweden and Finland. The incoherent scatter technique allows direct measurement of bulk plasma properties: electron density, ion temperature, electron temperature and plasma motion. For details about the incoherent scatter technique, see f.ex. Lehtinen and Huuskonen [1996], Nygrén [1996], and Wannberg *et al.* [1997]. In this thesis I've used pre-analyzed data or applied standard analysis to derive the plasma parameters from the raw radar observations.

The ESR has two parabolic dishes, one steerable and one fixed to point parallel to the F region geomagnetic field, see Figure 4.6. The steerable dish is 32 meters in diameter, and the fixed dish is 42 meters. The radar can operate both dishes at the same time.

5.2 All-sky cameras

The University of Oslo operates several all-sky cameras (ASC, also referred to as an All-sky Intensified Photometer (ASIP)) in the auroral zone. I have used the cameras located in Longyearbyen and Ny-Ålesund.

The cameras consist of fisheye optics with a 180° field of view and a filter wheel. The wheel switches automatically between different bandpass filters that only let a selected auroral wavelength through. A picture is taken for each filter wavelength one to three times per minute. The camera is equipped with an intensifier that allows photographing very weak aurora. These instruments cannot be operated in moonlight, as it would overwhelm and possibly damage the intensifier.

5.3 Meridional scanning photometers

A meridional scanning photometer (MSP) is an instrument that contains several photometers with narrow fields of view and a filter that only admits a selected auroral wavelength. The photometers are pointed at a rotating mirror that scans the field of view across the sky in a plane aligned with geomagnetic north (the magnetic meridian). The MSP has high resolution in time and space along the scan plane, and all wavelengths are observed simultaneously. Like the all-sky cameras, the MSP cannot operate in moonlight.

The University Center on Svalbard (UNIS) operates an MSP at the Kjell Henriksen Observatory (KHO), near the EISCAT site. It was originally located at the Auroral Station in Adventdalen, nearer to Longyearbyen. The KHO opened in 2008 and took over the Auroral Station's instruments.

The University of Oslo operated an MSP in Ny-Ålesund, at the Sverdrup Station, from 1998 to 2007.

5.4 Atmospheric models

Temperature and molecular composition of the neutral gas, and the composition of the ionosphere, are some parameters that aren't always possible to measure in real time. It is then necessary to rely on models for these parameters. I have used various iterations of the MSIS model [Hedin, 1987; Hedin, 1991; Picone *et al.*, 2002] for the neutral parameters. Mostly I have used MSIS-E-90 [Hedin, 1991], as it has a published scriptable web interface. I also used the 2012 version of the International Reference Ionosphere (IRI) model [Bilitza *et al.*, 2014] for ionospheric composition. These empirical models are based on satellite and ground-based datasets covering several solar cycles, but much of the data they are based on

come from lower and middle latitudes, and they may not be very accurate in polar regions [f.ex. Moen *et al.*, 2007]. The models are actively being developed and the number of ground-based and space-based instruments that can contribute to the models is ever increasing.

The IGRF geomagnetic field model has already been introduced in Chapter 3.

Part II

Summary

Chapter 6

Summary and conclusion

6.1 Paper abstracts

6.1.1 On the relationship between flux transfer events, temperature enhancements and ion upflow events in the cusp ionosphere

Full citation: Å. Skjæveland, J. I. Moen, and H. C. Carlson [2011]. On the Relationship between Flux Transfer Events, Temperature Enhancements and Ion Upflow Events in the Cusp Ionosphere. *J. Geophys. Res.* A10305. DOI: 10.1029/2011JA016480.

Abstract: A transit of the dayside aurora across the field-of-view of the EISCAT Svalbard Radar occurred on 20 December 1998. This offered an excellent opportunity to study the spatial structure of the cusp/cleft aurora using meridian scanning photometer and incoherent scatter radar. We were able to identify distinct regions of upflow driven by ion heating (type 1) and upflow driven by electron heating (type 2) around poleward-moving auroral forms, a transient auroral feature tied to flux transfer events. A quiet period before the auroral transit allowed us to estimate a neutral temperature profile, which enabled calculation of the ion-neutral relative wind. We found evidence for purely ion heating-driven upflow equatorward of the cusp auroral boundary, and for electron heating-driven upflow near the equatorward auroral boundary. The greatest upflow occurred near the center of the cusp aurora when both ion and electron temperatures were enhanced. The observed upflows were greater than expected from ambipolar diffusion alone, suggesting that ion-neutral frictional heating did contribute

to upflow events in most cases. The great variability observed in ion temperature indicates that the ion flow was greatly structured within the aurora. Type 1–2 upflows may be considered as spatial structures of active cusp. Upflows are observed at various times in their evolution, and one upflow event, estimated to be 5–10 minutes old, showed a lifting of the F region of some 100 km, indicating a hybrid of type 1 and type 2.

6.1.2 Which cusp upflow events can possibly turn into outflows?

Full citation: Å. Skjæveland, J. Moen, and H. C. Carlson [2014]. Which Cusp Upflow Events Can Possibly Turn into Outflows? *J. Geophys. Res. Space Physics* 119.8, 2013JA019495. ISSN: 2169-9402. DOI: 10.1002/2013JA019495.

Abstract: Two sequences, before and after magnetic noon, respectively, of poleward-moving auroral forms with associated upflows situated above the European Incoherent Scatter Svalbard Radar allowed close study of ion upflow dynamics. We find that flux intensity is correlated with plasma temperature and that upflowing plasma undergoes acceleration proportional to the slope of the velocity profile and to the velocity at each altitude. The potential for upflows to lift thermal plasma to regions where broadband extremely low frequency electric field activity can cause nonthermal acceleration leading to outflow is examined. Equations for estimating the travel time of upflowing plasma are presented. We find that around 40% of the observed upflow profiles with a unit number flux greater than $1 \times 10^{13}\,\mathrm{m^{-2}\,s^{-1}}$ can transport plasma from 500 to 800 km altitude in less than 10 min, approximately the typical lifetime of pulsed upflow events. Almost all such profiles can transport plasma from 600 to 800 km in the same time span. Typical transport times for other altitude ranges are also presented. Post magnetic noon the background electron density was somewhat higher than prenoon due to transport of EUV-enhanced plasma, and the postnoon ion flux was somewhat weaker than prenoon.

6.1.3 A statistical survey of heat input parameters into the cusp thermosphere

Full citation: Å. S. Skjæveland, H. C. Carlson, and J. Moen [2017]. A Statistical Survey of Heat Input Parameters into the Cusp Thermosphere. Submitted to Journal of Geophysical Research Space Physics.

Abstract: Based on three winters of observational data, we present those ionosphere parameters deemed most critical to realistic space weather ionosphere and thermosphere representation and prediction, in regions impacted by variability in the cusp. The CHAMP spacecraft revealed large variability in cusp thermosphere densities, measuring satellite drag enhancements exceeding 20% half the time, including up to doublings. The community, while still seeking consensus on driving mechanisms, recognizes clear need for more realistic representation of plasma flow-speeds [flow-jets] and electron density profiles [conductivities] near the cusp [correlation studies]. Existing average-value models produce order of magnitude errors in these parameters, resulting in unacceptably large underestimations of predicted drag. Herein we fill this critical knowledge gap with statistics-based specification of these key parameters over their range of observed values. The EISCAT Svalbard Radar [ESR], when within reach of the cusp, tracks plasma flow V_i, electron density N_e, and electron, ion temperatures T_e, T_i, with consecutive 2–3 minute windshield-wipe azimuth scans of 1000 × 500 km areas, elevation scans doing likewise. Critically, staring parallel to Earth's magnetic field lines it can measure high-resolution profiles of these plasma parameters. Deriving statistics on these parameters for conductivities and plasma flow fields, we enable derivation of thermosphere heating rate profiles under background and frictional-drag-dominated magnetic reconnection driven flow-jet conditions. Use of our new data-based parameter inputs can make *order of magnitude* corrections to *input* data driving thermosphere models, enabling removal of previous two-fold drag errors.

6.2 Summaries

Figure 6.1 shows the intrument configuration used in paper 1, 2 and parts of 3. A 630.0 nm all-sky image is projected to 250 km altitude and shown on a map. On this image is drawn a line showing the scan plane of the Ny-Ålesund MSP, with north and south zenith angles in the MSP field of view indicated. The red dot is the location of the MSP and all-sky camera, and the white dot is the location of the field-aligned ESR beam at 250 altitude, located at 32° south zenith angle in the MSP view. The figure shows an auroral form located overhead in Ny-Ålesund and poleward of the MSP beam.

Figure 6.2 illustrates the field-aligned radar mode, used in all three papers. This mode is useful since all the plasma in the beam is subject to the same magnetopause inputs, and the resulting structures in the ionosphere are field-aligned.

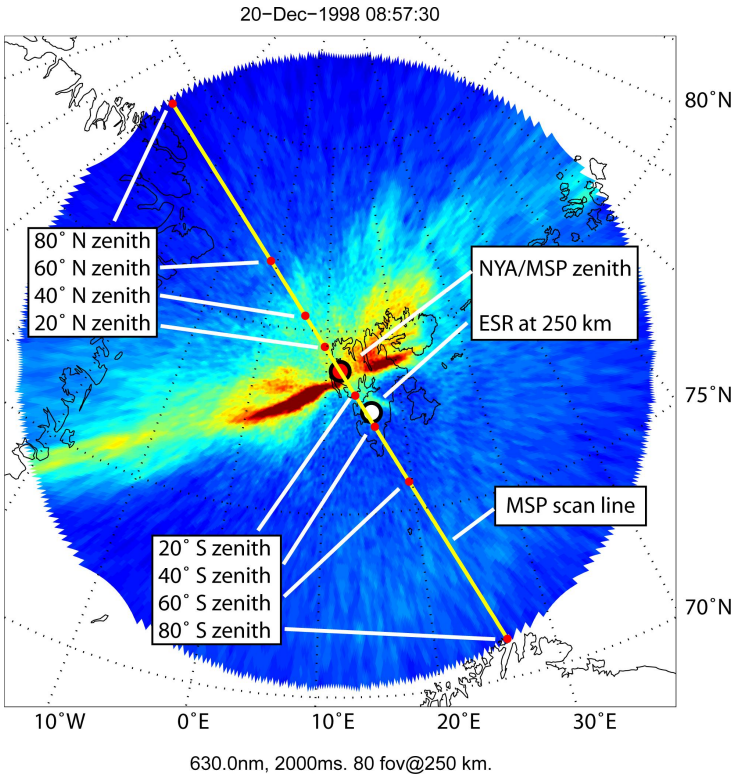

Figure 6.1: Scan plane of the Longyearbyen MSP and a Ny-Ålesund ASC image of red cusp aurora, projected to 250 km altitude. MSP zenith angles and location of ESR beam indicated (beam width not to scale).

A disadvantage compared to f. ex. a northward-pointing beam is that the evolution of individual flux tubes can't be observed.

6.2.1 Paper 1: Ion upflows

To determine the main drivers of cusp ion upflow, we carried out a case study of the dayside aurora on 20 December 1998. The data used are: field-aligned radar data from the ESR, MSP data from Ny-Ålesund, and ASC images from Ny-Ålesund. Optical data from Longyearbyen were available, but not useful due to haze and clouds.

Figure 6.3 shows the radar and MSP data used in paper 1, divided into five regions R1–R5, based on observed characteristics of upflow, and T_i and T_e enhancements. Four upflow and heating events are labelled E1–E4. Figure 6.4 shows a zoomed-in view of the same data.

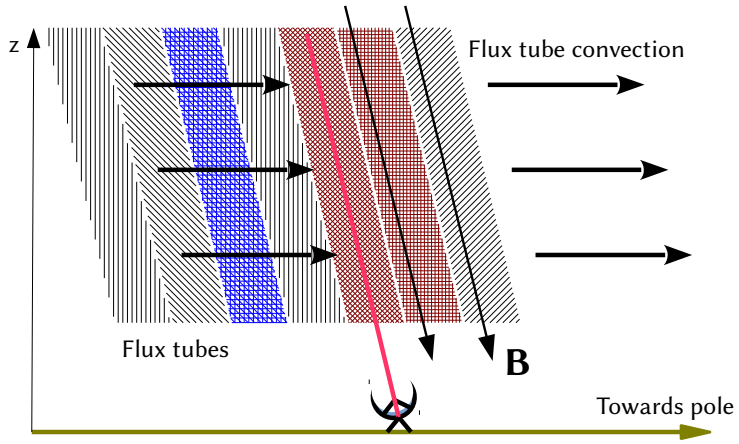

Figure 6.2: Illustration of the field-aligned radar mode. The radar beam is held parallel to the geomagnetic field ($\mathbf{B}$) while the ionospheric plasma convects across it. The different colors and patterns indicate that frozen-in plasma on nearby flux tubes can have quite different properties, for example high or low electron densities and electron/ion temperatures. These different properties are observed as time variations when the flux tubes are transported across the radar beam by $\mathbf{E} \times \mathbf{B}$ drift.

The paper carries out a minute-by-minute examination of the relationship between poleward-moving auroral forms (PMAFs), ion and electron gas heating, and ion upflow. The paper describes ion upflows observed on 20 December 1998 by the Eiscat Svalbard Radar. The dayside aurora moved across the radar beam as the polar cap shrank and grew due to unbalanced dayside- nightside reconnection. The paper focuses on a transit during an equatorward expansion of the auroral arc from 08:45 UT to 09:45 UT (see MSP data in Figure 6.3E). As the aurora moved equatorward, it brightened and launched a series of PMAFs, which have been previously identified as signatures of flux transfer events [Moen *et al.*, 2004a], i.e. discrete reconnection events. Strong ion and electron heating well as simultaneous upflow was observed when these PMAFs transited the radar beam. The link between upflows and PMAFs in this dataset was explored by Moen *et al.* [2004a]. We investigate the drivers of ion upflow through electron and ion heating in this paper, identifying one type 1 upflow and several type 2 outflows [Wahlund *et al.*, 1992], as well as noting that upflows may well contain the characteristics of both types.

The paper also estimates the ion-neutral velocity shear ($\Delta v = |\mathbf{v}_i - \mathbf{v}_n|$) from the ion temperature enhancement ($\Delta T = T_i - T_n$) using Equation 2.9 and discusses

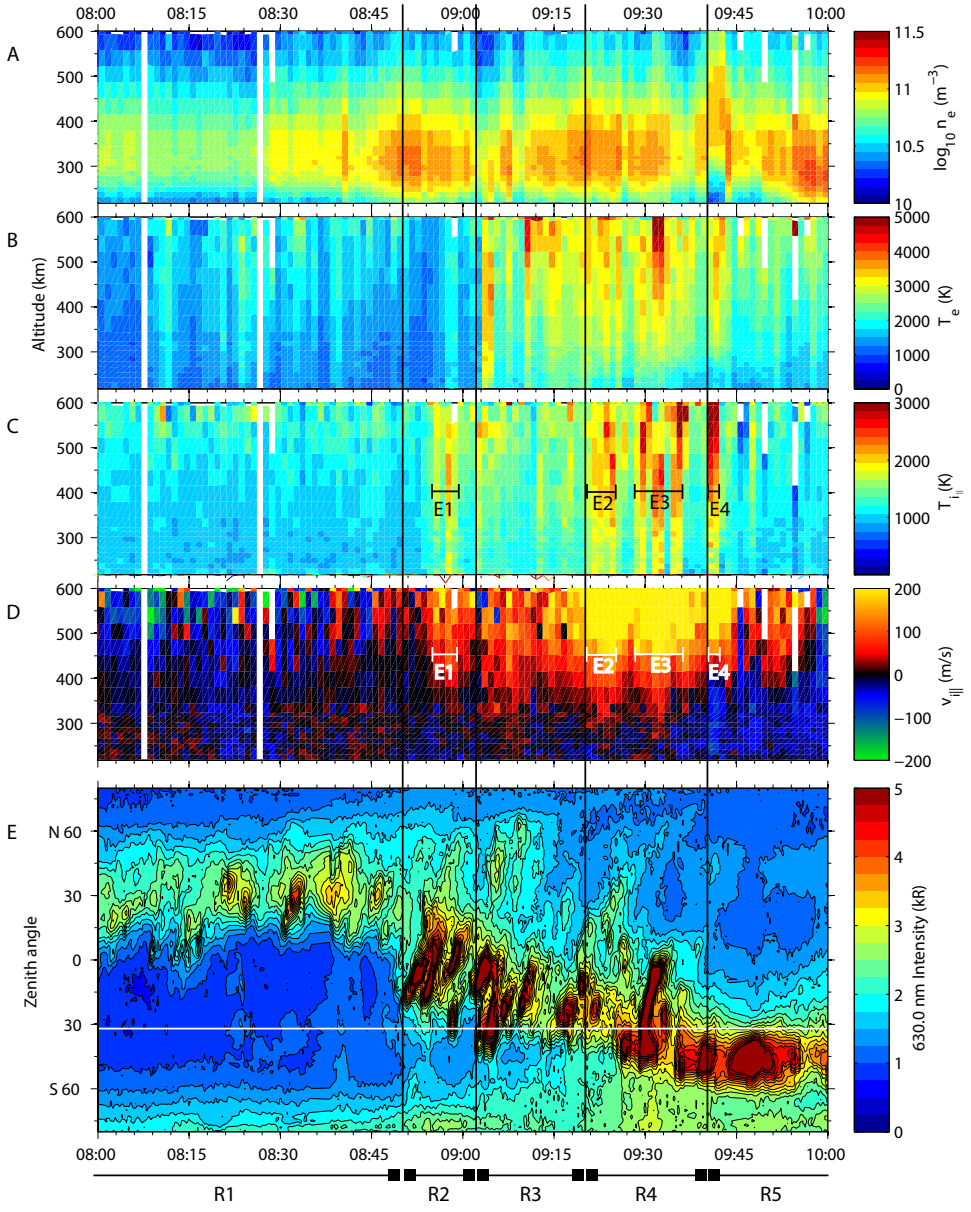

Figure 6.3: Figure 2 from paper 1. Panels A–D show field aligned radar data: A) electron density ($\log_{10}$ scale), B) electron temperature, C) ion temperature, D) ion line-of-sight velocity. Panel E) shows 630.0 nm MSP data from Ny-Ålesund, with location of ESR beam at 250 km altitude marked by white line. Regions R1–R5 are marked on the bottom of the figure, with vertical black lines marking borders between regions. Ion heating events E1–E4 are marked in panels C and D.

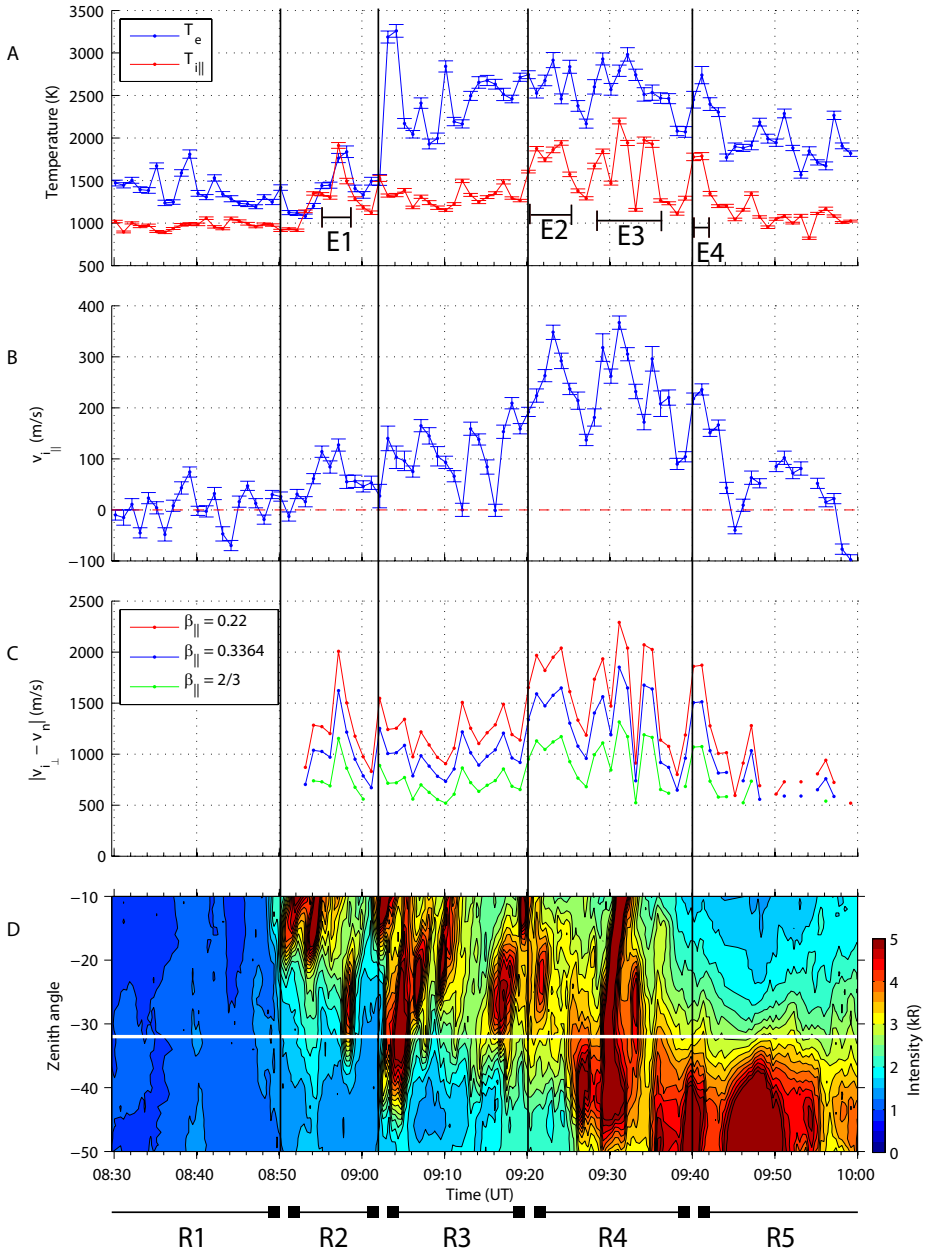

Figure 6.4: Figure 4 from paper 1. Panels A–B show field-aligned radar data from selected altitudes: A) shows ion and electron temperatures at 300 km, B) shows ion line-of-sight velocity at 490 km. C) shows ion-neutral velocity shear calculated for three different values of ion temperature anisotropy. D) shows Ny-Ålesund MSP data for 630.0 nm emissions. Regions and events as in Figure 6.3.

Table 1. Travel Times and Percentages of Events With Travel Times Less Than 10 min for Observed Strong Flux Profiles[a]

From Altitude (km)	Travel Time to 600 km (min)	Percentage Less Than 10 min	Travel Time to 800 km (min)	Percentage Less Than 10 min	Travel Time to 1000 km (min)	Percentage Less Than 10 min
400	10–25 [12–25, 16#]	6 [0]	15–30 [19–33, 8#]	0 [0]	17–35 [n/a, 0#]	0 [n/a]
450	5–15 [6–15, 43#]	57 [60]	10–25 [12–20, 28#]	8 [0]	12–25 [15–22, 21#]	0 [0]
500	3–8 (2–7) [3–8, 53#]	95 (97) [98]	6–15 (6–16) [8–17, 38#]	42 (44) [23]	9–23 (7–21) [12–19, 29#]	11 (16) [0]
550	2–4 (1–3) [1–4, 64#]	100 (100) [100]	4–12 (4–12) [5–13, 49#]	76 (79) [77]	7–17 (6–18) [9–17, 37#]	34 (39) [13]
600			3–10 (3–9) [4–9, 53#]	97 (96) [100]	5–14 (4–15) [6–14, 45#]	57 (63) [71]
700			1–4 (1–4) [2–4, 63#]	100 (100) [100]	3–10 (2–10) [4–9, 53#]	97 (93) [100]
800					2–6 (1–6) [2–5, 60#]	100 (99) [100]

[a]Numbers show travel time ranges and percentages for v_i fit, time-independent assumption (flux fit, time-independent assumption) [v_i fit, time-dependent assumption]. Number marked # in brackets is the number of travel time data points for that altitude range for the time-dependent calculations. The time independent assumption moves with the flux tube and satisfies conservation of flux; the time dependent applies flux tube data only while overhead within the radar field of view. The time ranges exclude the longest 5% of travel times; see text. Flux fit is not calculated for 400 and 450 km starting altitudes.

Table 6.1: Table 1 from Skjæveland *et al.* [2014], showing calculated travel times of upflowing plasma to and from various altitudes, for three different models of upflow. See paper for details.

the problem of ion temperature anisotropy, i.e. the possibility that the ion thermal velocity distribution is not spherical but elongated in the direction orthogonal to the magnetic field [McCrea *et al.*, 1993; St.-Maurice and Schunk, 1977]. The paper shows calculations for the ion-neutral velocity shear deduced from the ion temperature for varying degrees of anisotropy (Figure 6.4C), with no anisotropy giving the lowest Δv. We do not discuss the issue of anisotropy in the other papers, implictly assuming no anisotropy.

The conclusion of the paper is the following observations:

1) A type 1 upflow was observed when the aurora was just poleward of the radar beam, and outside the auroral precipitation. When the beam was within the auroral oval but T_i was not significantly elevated, the observed type 2 upflow was comparable to that predicted by ambipolar upflow alone. Elevated T_i was connected with auroral transients.

2) The strongest upflows were observed within the auroral transients, when both T_i and T_e were elevated. The peak flows were not centered in the auroral transients, but near their edges, consistent with the Southwood [1987] FTE model.

3) the ion flow in and around the aruroral transients is fine-structured, consistent with narrow plasma flow channels set up by flux transfer events.

6.2.2 Paper 2: Upflows that feed outflows

This paper attempts to answer the question "Which cusp upflows can reach outflow energization altitudes?". To do this, we look again at the data from 20 De-

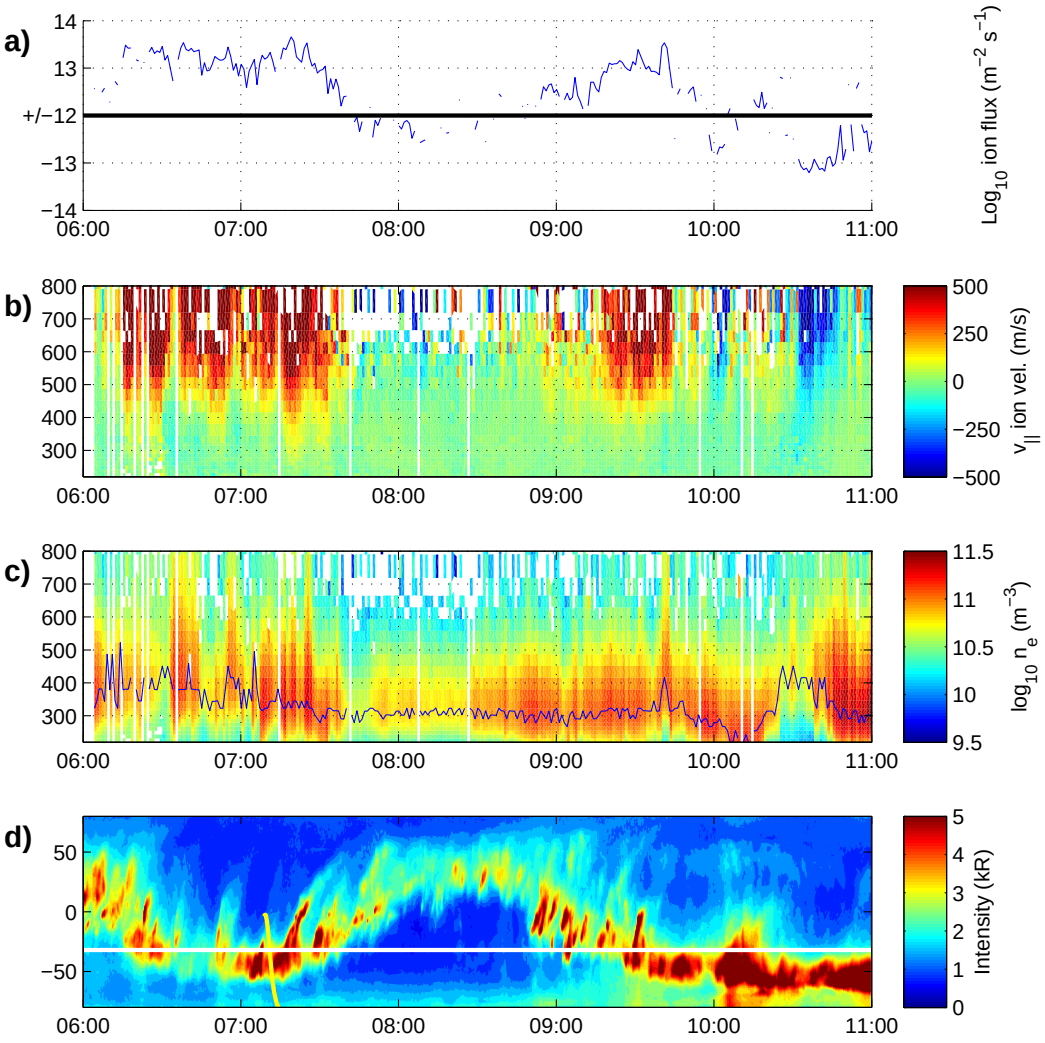

Figure 6.5: Figure 1 from paper 2. The panels show A) positive and negative $\log_{10}$ ion number flux density, B) ion line-of-sight velocity, $\log_{10}$ electron density with altitude of density maximum shown by blue line, and D) 630.0 nm (red aurora) MSP data from Ny-Ålesund, with white line indicating location of the ESR beam at 250 km altitude, and yellow curve indicating a close passage of DMSP F13.

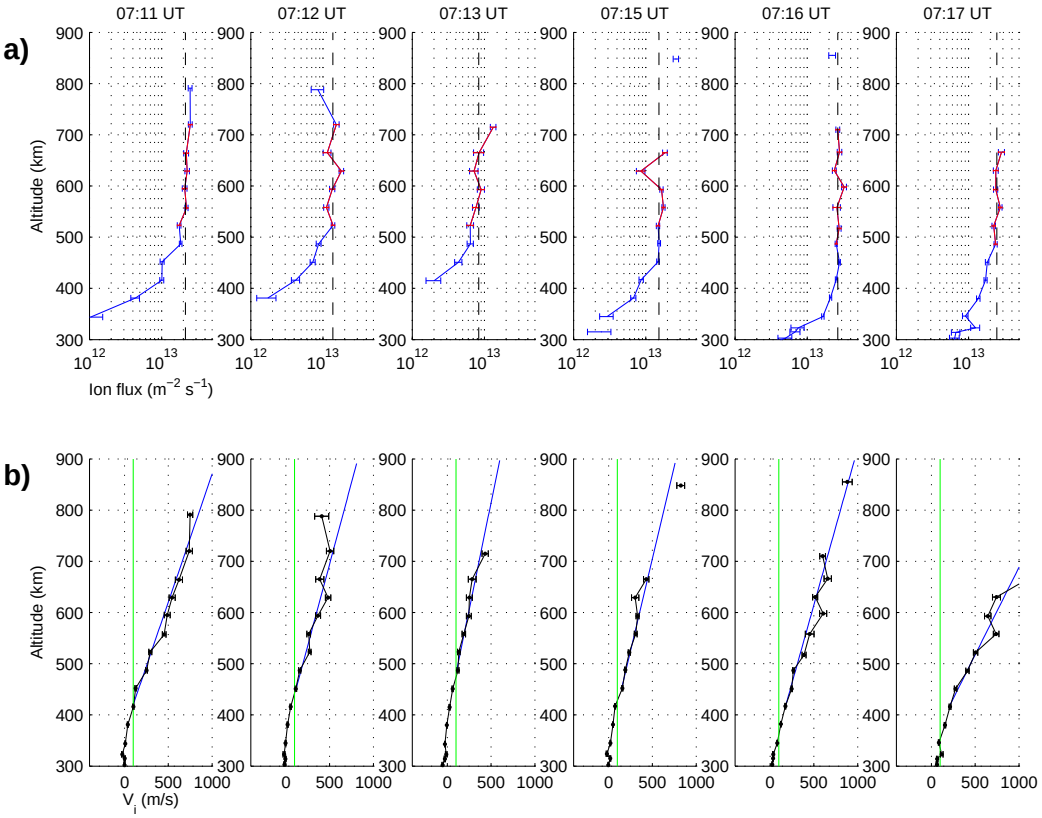

Figure 6.6: Figure 4 from paper 2. A) shows a sequence of ion flux profiles (the effect of the diverging geomagnetic field has been removed) approaching a constant value (dashed line) with increasing altitude. Points marked in red are used to compute constant-flux value. B) shows the ion line-of-sight measurements for the same times, and a linear fit to the velocity profile. Green line marks 100 m/s, the upflow threshold defined by Ogawa *et al.* [2009].

cember 1998, but this time we look at the ion number flux density (shorthand "ion flux") along the magnetic field. We examine the ion flux and bulk upflow of plasma to find travel times to altitudes where nonthermal processes may energize the plasma and create outflow, quantify the expected transport time for three different models of upflow.

The data used are: field-aligned radar data, Ny-Ålesund MSP, DMSP F13 ion flow data. The DMSP ion data are used to verify that the ion flux measured by ESR, at the furthest edge of its field of view, is in agreement with the ion flux measured in situ by the DMSP spacecraft. Figure 6.5 shows the measured ion flux and overview plots of MSP and radar data.

Where paper 1 looked at upflows event by event, this paper takes a statistical approach. We describe the typical characteristics of the flux we observe within upflow events: When the ion flux exceeds 1×10^{13} m^{-2} s^{-1}, the flux is typically fairly constant with altitude (implying that the upflow does not change the plasma density) from ~100–200 km above the F2 n_e maximum and to the end of the radar field of view. The flux increases significantly with altitude from the n_e maximum and up to 100–200 km above, and we name this the "source region", since the increase in ion flux with altitude means that plasma is leaving this region and being transported upwards, and the lost plasma is not fully replaced from below. Figure 6.6 shows examples of ion upflows and the corresponding ion fluxes.

Theoretically, the topside ion number flux per unit *magnetic flux* should be constant with altitude. Since the geomagnetic field diverges as the altitude increases (the flux tubes widen), this means that the ion number flux per unit *area* decreases with altitude. To simplify the figures and calculations, we have scaled all measured ion fluxes as if the geomagnetic field didn't diverge, using the geomagnetic field strength at 500 km altitude as the reference point.

Since the radar beam is static we cannot track the complete evolution of individual upflow events. All we have is a cross section as the event travelled across the radar beam. We therefore defined three independent ways of calculating how far the plasma will travel in an upflow event, based on three different sets of assumptions for the upflow structure and evolution. The resulting travel times are listed in Table 6.1, and they are in good agreement with each other.

We searched the literature for likely energy sources, and found that the broadband extremely low frequency (BBELF) waves in the topside ionosphere was a good candidate. Such waves are very common above ~1000 km, but common down to 800 km and have been observed as low as 600 km. The BBELF phe-

nomenon is not sharply defined, but is, essentially, any broad-spectrum oscillation of the local electric field from a few Hz up to 10–100 kHz depending on the study. As such, it is a "grab-all" term for topside electromagnetic wave activity, whatever the energy source of the wave.

The conclusion of the paper is: Assuming that the lifetime of an upflow event is comparable to that of a PMAF (8–10 minutes), we found that it was very unlikely that plasma from around 400 km altitude would be transported to above 800 km altitude, a likely region for outflow energization. However, plasma from 600 km or above would easily be transported 200 km or more into altitudes where outflow energizations are increasingly likely.

In the appendix, we make note of the empirical observation that ion velocity profiles within upflows tend to increase approximately linearly with altitude, and we derive equations of motion for upflowing plasma parcels based on this empirical observation.

6.2.3 Paper 3: Cusp heating: How often, how strong

This third paper focuses on the question "What are the actual energy deposition rates in the dynamic cusp?". We attempt to quantify the ion-frictional part of the energy deposition. To find this it is necessary to know the inputs to Equation 2.11. The plasma density and the ion temperature T_i are measured directly, the rest must perforce be taken from models.

The data used are: ESR field-aligned mode and scanning mode. Ny-Ålesund ASC and MSP and Longyearbyen MSP quicklooks were used to verify that the field-aligned radar beam was within or near the cusp aurora at least some of the time for each day analysed, although periods of each day without optical data were also used.

Rather than just computing energy rates minute by minute, we wanted statistics of how common ion-frictional events in the cusp are, as well as separate typical deposition rates for when the cusp was reconnection-enhanced and when it was quiescent.

Dayside reconnection, with its softer electron precipitation and absent or faint E layer, will deposit its energy in the thermosphere differently than in the night-side. At night the direct precipitation as well as the ionization will be focused on the E region, while for the dayside both will be higher up and spread over a larger altitude range (see Section 4.7, particularly Figures 4.10 and 4.11). Carlson *et al.* [2012] demonstrated that the thermospheric effect of a given en-

ergy input was strongly dependent on altitude, and that dayside reconnection could cause the neutral upwelling observed by CHAMP when the energy deposition occurred at 170–200 km altitude rather than ~125 km as is typical on the nightside.

A scanning mode of the ESR was used to gather statistics on the rate of occurence of reconnection in the cusp, using structured enhanced ion temperature as a proxy for reconnection. Figure 6.7 shows a scan in elevation, where the scanning plane is aligned with the magnetic meridian. The T_i panel shows two ion heating events, a weaker between 74° and 75° magnetic latitude (MLAT), and a stronger between 77°–78° MLAT. The enhanced T_e north of 74° MLAT indicates that this region is on open field lines. The scanning mode does not have sufficient resolution to study n_e enhancements below 200 km.

Figure 6.8 shows a different scanning setup where the elevation is held constant and the beam is moving in azimuth, sweeping a conical surface. Here an ion heating event can be identified at 74° MLAT, in the middle of a transient plasma flow channel 200 km wide.

From these scanning data, we recorded the largest observed T_i in each scan and compiled statistics of heating events in/near the cusp. The result is shown in Figure 6.9A, with B showing the same statistic computed using field-aligned data for comparison. This statistic tells us how common heating events are; field-aligned data underestimate this because many heating events transit rapidly across the radar beam or do not cross the radar beam at all.

Further, six days of field-aligned ESR data from the cusp in winter near solar maximum were analyzed. The precice times when the radar beam was in the cusp were identified, primarily from the radar signatures of the cusp. We then divided the cusp into “quiescent” and “reconnection-enhanced” states. Figure 6.10 shows the statistical profiles and the distribution of the radar data. Also shown are model n_e (IRI) and T_n (MSIS) profiles. The IRI model T_i profile (not shown) was practically identical to the MSIS T_n profile.

It turned out that because of the geometry and timing of the ionospheric signature of reconnection events, while n_e (below ~200 km) and T_i (throughout the F region) will both be enhanced, the two enhancements do not quite overlap in space and time, and the narrow field-aligned radar beam would frequently only see one or the other of the enhanced signatures. We therefore made two independent sets of “quiescent” and “reconnection-enhanced” data; one for n_e and one for T_i. Figure 6.10 shows the resulting profiles for n_e and T_i, both quiescent and enhanced.

The result of this paper is 1) the statistics of ion heating events in the cusp, observed by scanning-mode radar, from which reconnection rate and magnitude can be inferred, and 2) representative electron density and ion temperature profiles for quiescent and active cusp. The results for 1) are shown in Figure 6.9, where similar statistics for field-aligned data are shown for comparison. As we expected, the scanning-mode finds heating events in the cusp significantly more often than a static field-aligned beam. Results for 2) are shown in Figure 6.11, with deposition rates according to Equation 2.11 for a range of plausible ion-neutral plasma drifts shown in Figure 6.12. Of particular note is the IRI2012 model n_e profile, which is a different shape than and around an order of magnitude less than the empirical profiles. As a consequence, energy deposition rates computed using this model profile will also be low by an order of magnitude.

6.3 Conclusion

I opened this thesis with three science questions:

1. What are the major drivers for cusp ion upflows?
2. Which cusp upflows can reach outflow energization altitudes?
3. What are the actual energy deposition rates in the dynamic cusp?

We have presented a paper to answer each question. Paper 1 analyzed cusp upflow drivers in detail, separating the ambipolar flow from the ion-heating-driven upwelling and teasing out information about the internal flow structure in the upflow and heating events. The strongest upflows occur when both T_e and T_i are enhanced, and occur near the edges of auroral forms rather than their center.

Paper 2 then found that the studied upflows were fully able to lift plasma from 600 to 800 km in their lifetime, providing a source of fresh plasma to the nonthermal energization mechanisms on the top of the ionosphere. The upflow would draw plasma from the region between ~300–450 km while doing so.

Paper 3 presents empirical profiles of electron density and ion temperature when the cusp ionosphere (below 200 km) is reconnection-enhanced vs. quescent. This is a vital input to models seeking to reproduce the thermospheric upwelling in the cusp first seen by the CHAMP spacecraft. The paper also presents data on how often heating events able to cause such upwellings occur: knowledge of this is essential in modelling the occurrence rate of the thermospheric upwelling and its effect on low-orbiting spacecraft.

These three papers collectively add to the available knowledge of vertical transport in the cusp, enabling better modelling and forecasting of the dayside ionospheric weather. This is relevant to radio communications and precise navigation in polar regions as ionospheric activity can cause strong gradients and turbulence in the ionosphere, modifying radio signals.

6.4 Future work

Possible future work include collecting more statistics on the cusp upflow and heating phenomena studied here, for the purpose of real-time prediction of upflow and upwelling. The work here uses a few days of data under quiet to moderately active conditions. To include accurate model profiles in general-purpose ionospheric models it is necessary to gather a large volume of cusp data over a wide range of ionospheric activity levels, sunspot numbers and all seasons. Dedicated long-term radar runs such as the International Polar Year runs will be necessary.

Volumetric radar such as the existing Advanced Modular Incoherent Scatter Radar (AMISR) facilities in North America and, in the longer term, the EISCAT_3D radar facilities with overlapping fields of view planned in northern Scandinavia, will greatly increase knowledge of heating and upflow phenomena, by measuring the whole event throughout its lifetime. Unfortunately EISCAT_3D won't see the cusp over Svalbard, and there are as of yet no plans to build volumetric ISR on Svalbard. Volumetric measurements of sunlit cusp from AMISR should be transferable to Svalbard, but ESR remains alone in being able to observe the dark midwinter cusp.

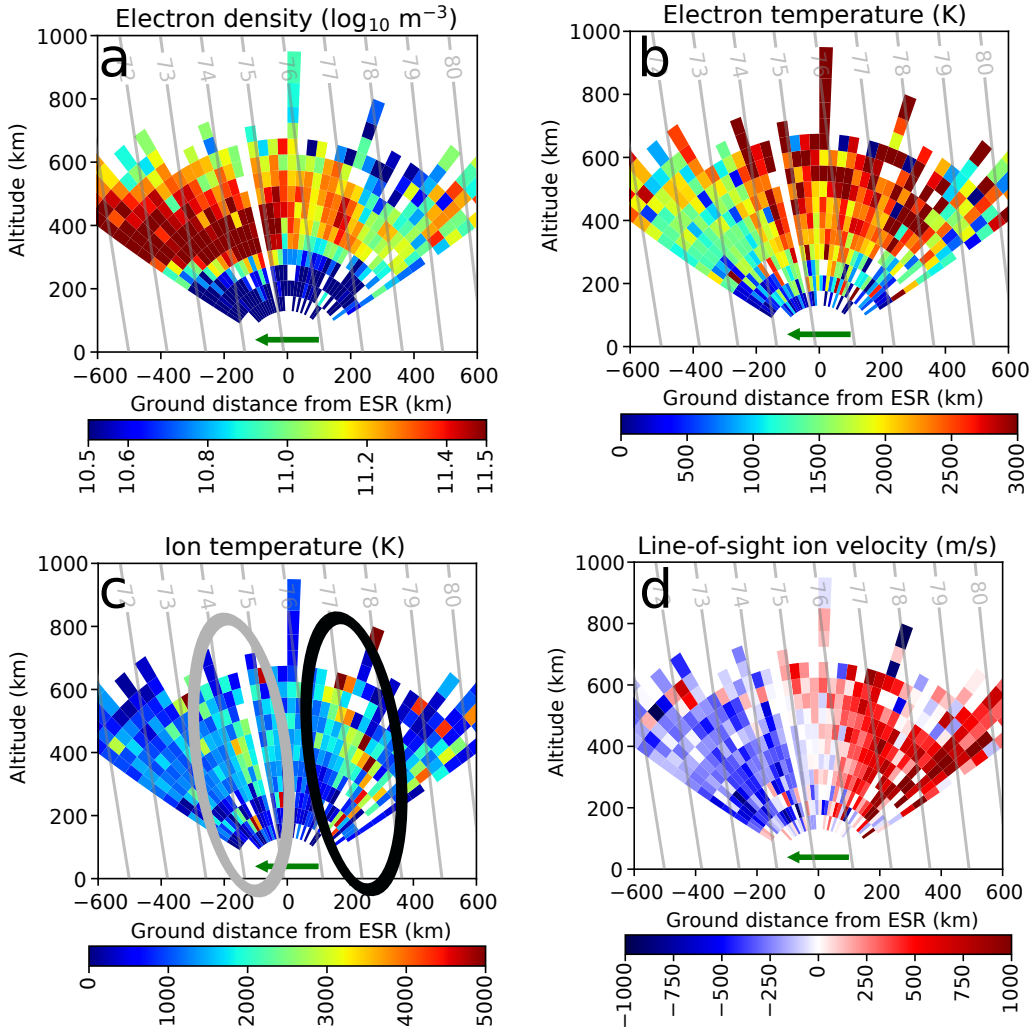

Figure 6.7: Figure 2 from paper 3. Example of elevation scanning mode of the ESR. The gray lines indicate AACGM MLAT (parallel to the geomagnetic field). The arrow below the radar fan shows direction of radar beam motion. Electron temperature indicates that 74° MLAT and north are on open field lines. Two ion heating events are observed in subfigure c: a lesser at 74°–75° (ringed in grey) MLAT and a greater at 77°–78° MLAT (ringed in black).

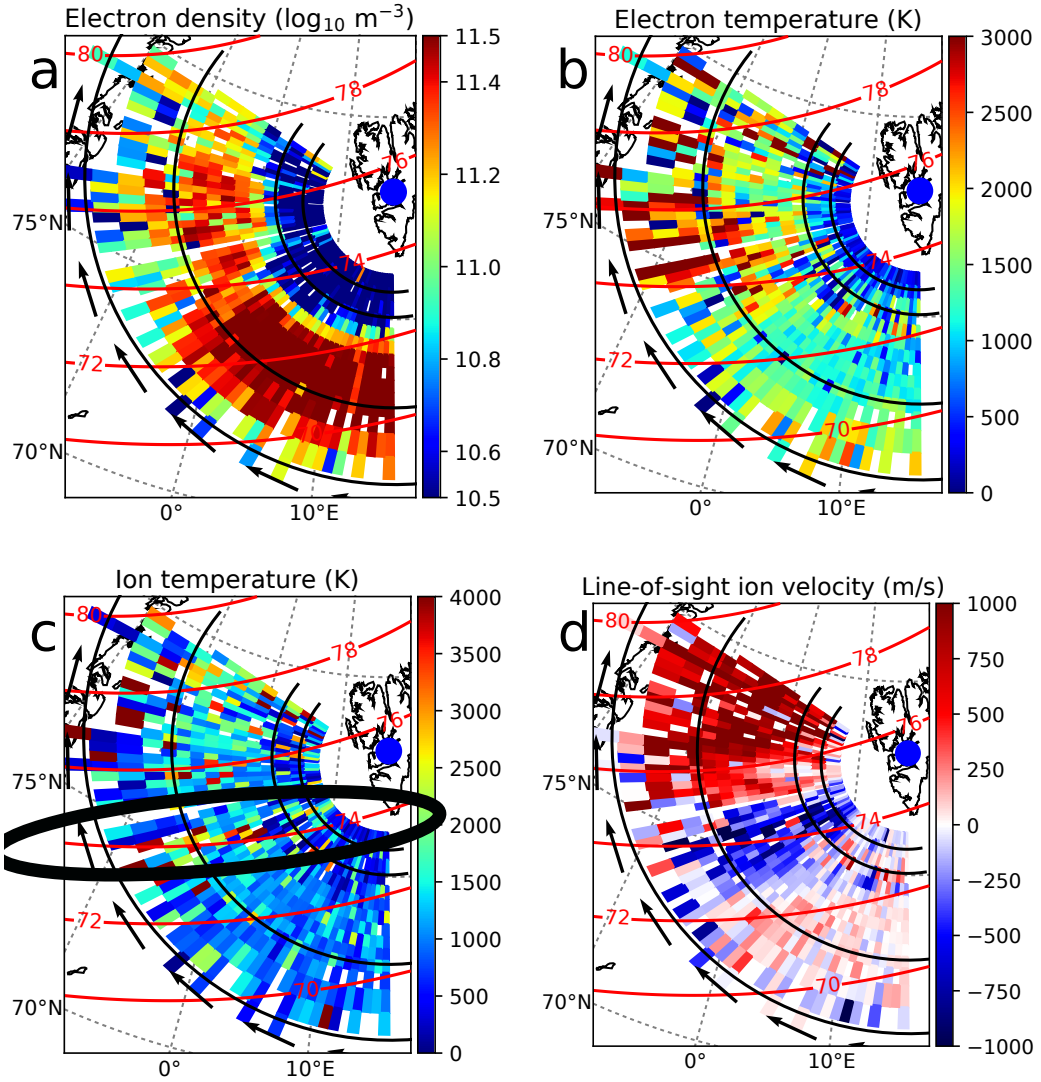

Figure 6.8: Figure 3 from paper 3. Example of azimuth scanning mode of the ESR. Red lines indicate AACGM MLAT. Black arrows show direction of radar beam motion. Black lines indicate altitudes (150, 200, 400, 600 km). An MLAT-aligned ion heating event is ringed in black at 74° MLAT.

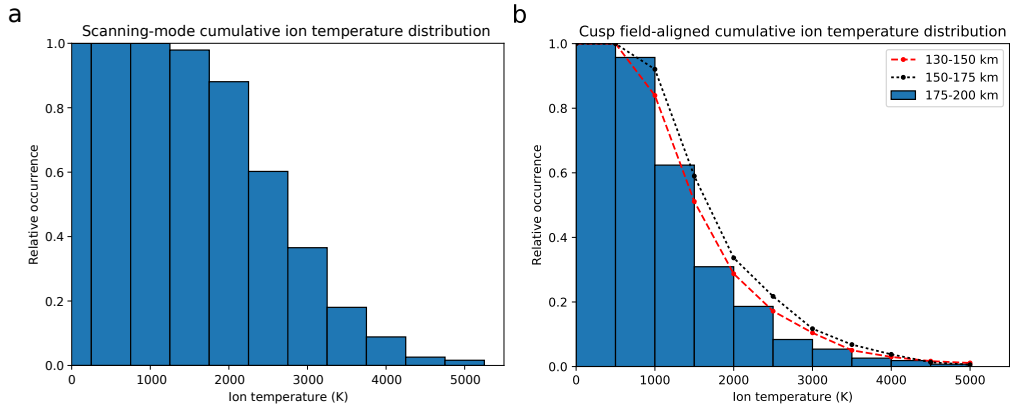

Figure 6.9: Figure 17 from paper 3. A) T_i heating occurrence rate from scanning-mode data, in the form of a cumulative histogram. Bar x shows the occurrence rate of temperatures x K or higher. B) shows the same calculation, done for field-aligned cusp data and several altitude ranges.

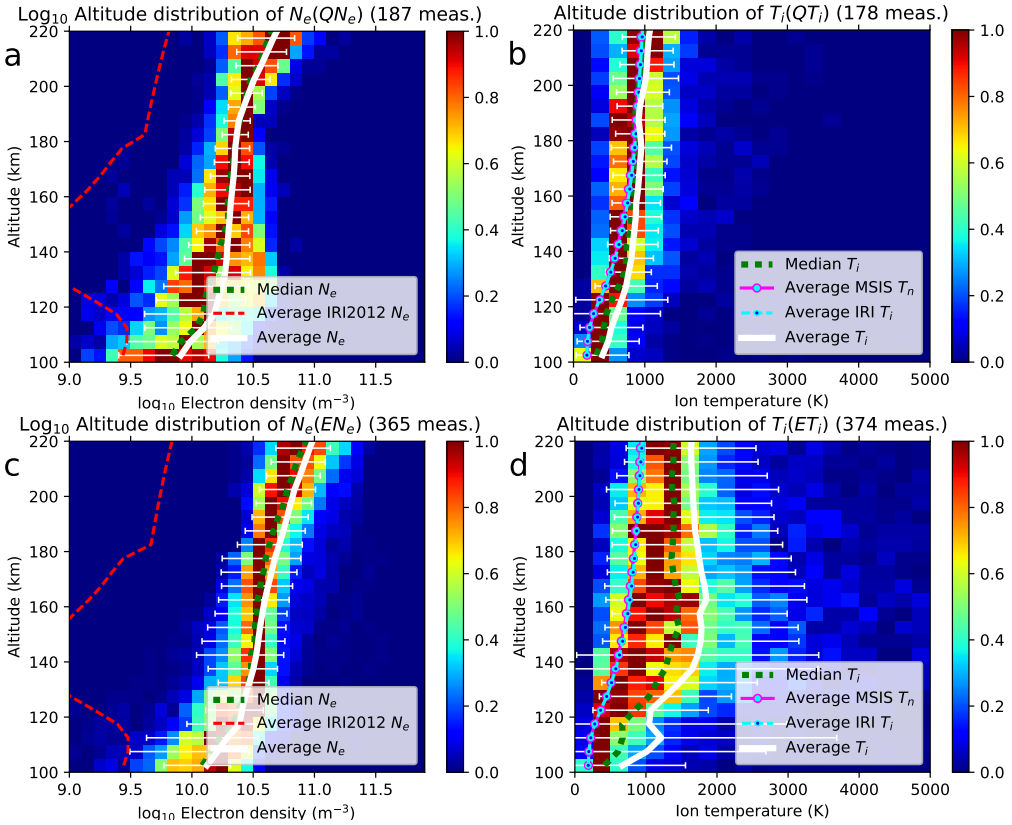

Figure 6.10: Figure 7a, c; 9b, d from paper 3. Statistical profiles for n_e and T_i, on top of the data used to compute them. Left column shows n_e data, right column shows T_i data. Top row shows quiescent data, bottom row shows enhanced data. Both median and averages are shown, as well as IRI2012 n_e and T_i and MSIS T_n. The model T_n and T_i are practically identical.

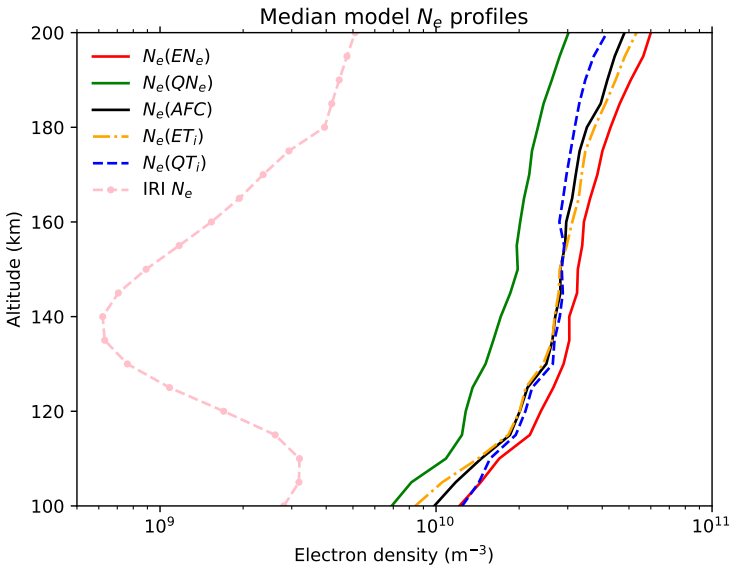

Figure 6.11: Figure 14 from paper 3. Statistical n_e profiles. From top of legend: computed n_e for enhanced n_e, quiescent n_e, all field-aligned cusp data, enhanced T_i, quiescent T_i, IRI2012 n_e.

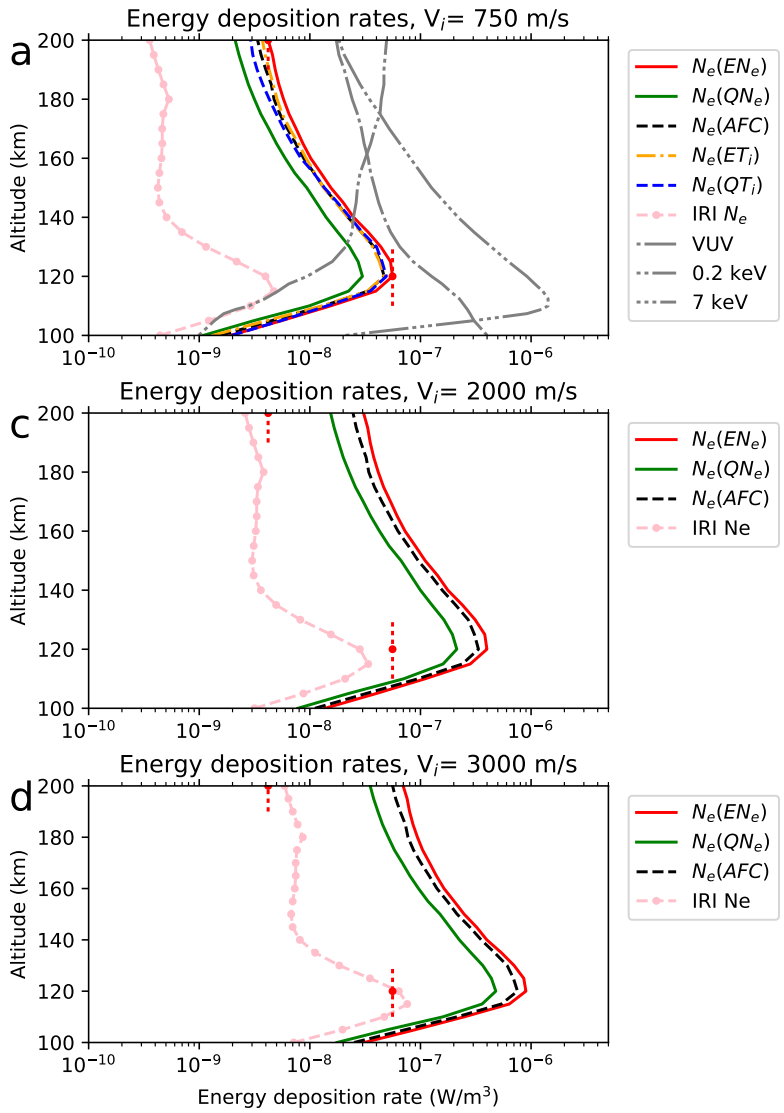

Figure 6.12: Figure 15a, c, d from paper 3. a shows heating deposition rates using all statistical n_e profiles for Δv = 750 m/s, and gray curves show VUV and particle precipitation energy depositions from Thayer and Semeter [2004]. c, d show deposition rates for selected n_e profiles for Δv =2000/3000 m/s. The red vertical markers indicate the positition of the 200-km value and peak value of the n_e profile labelled "$N_e(EN_e)$" in A).

Bibliography

Alfvén, H. (1942). On the Existence of Electromagnetic-Hydrodynamic Waves. *Ark. För Mat. Astron. Och Fys.* 29B.2, pp. 1–7.

Baker, K. B. and S. Wing (1989). A New Magnetic Coordinate System for Conjugate Studies at High Latitudes. *J. Geophys. Res.* 94 (A7), pp. 9139–9143. ISSN: 2156-2202. DOI: 10.1029/JA094iA07p09139.

Baron, M. J. and R. H. Wand (1983). F Region Ion Temperature Enhancements Resulting From Joule Heating. *J. Geophys. Res.* 88 (A5), pp. 4114–4118. ISSN: 2156-2202. DOI: 10.1029/JA088iA05p04114.

Bilitza, D., D. Altadill, Y. Zhang, C. Mertens, V. Truhlik, P. Richards, L.-A. McKinnell, and B. Reinisch (2014). The International Reference Ionosphere 2012 – a Model of International Collaboration. *J. Space Weather Space Clim.* 4, A07. ISSN: 2115-7251. DOI: 10.1051/swsc/2014004.

Bjoland, L. M., X. Chen, Y. Jin, A. S. Reimer, Å. Skjæveland, M. R. Wessel, J. K. Burchill, L. B. N. Clausen, S. E. Haaland, and K. A. McWilliams (2015). Interplanetary Magnetic Field and Solar Cycle Dependence of Northern Hemisphere F Region Joule Heating. *J. Geophys. Res. Space Physics* 120.2, 2014JA020586. ISSN: 2169-9402. DOI: 10.1002/2014JA020586.

Brekke, A. (1997). Physics of the Upper Polar Atmosphere. 1st ed. Wiley-Praxis Series in Atmospheric Physics. John Wiley & Sons Ltd, Praxis Publishing Ltd. ISBN: 0-471-96018-7.

Brekke, A. (2013). Physics of the Upper Polar Atmosphere. Springer Atmospheric Sciences. Berlin, Heidelberg: Springer Berlin Heidelberg. ISBN: 978-3-642-27401-5. DOI: 10.1007/978-3-642-27401-5.

Burchill, J. K., D. J. Knudsen, B. J. J. Bock, R. F. Pfaff, D. D. Wallis, J. H. Clemmons, S. R. Bounds, and H. Stenbaek-Nielsen (2004). Core Ion Interactions with BB ELF, Lower Hybrid, and Alfvén Waves in the High-Latitude Topside Ionosphere. *J. Geophys. Res. Space Phys.* 109 (A1). 00013, A01219. ISSN: 2156-2202. DOI: 10.1029/2003JA010073.

Carlson, H. C., T. Spain, A. Aruliah, Å. Skjæveland, and J. Moen (2012). First-Principles Physics of Cusp/Polar Cap Thermospheric Disturbances. *Geophys. Res. Lett.* 39.19, p. L19103. ISSN: 0094-8276. DOI: 10.1029/2012GL053034.

Chamberlain, J. W. (1961). Physics of the Aurora and Airglow. Special Publications. Reprinted 1995, online 2013. Washington, D. C.: American Geophysical Union. 704 pp. ISBN: 978-0-87590-857-1. DOI: 10.1029/SP041.

Cousins, E. D. P. and S. G. Shepherd (2010). A Dynamical Model of High-Latitude Convection Derived from SuperDARN Plasma Drift Measurements. *J. Geophys. Res. Space Phys.* 115 (A12), A12329. ISSN: 2156-2202. DOI: 10.1029/2010JA016017.

Cowley, S. W. H. and M. Lockwood (1992). Excitation and Decay of Solar Wind-Driven Flows in the Magnetosphere-Ionosphere System. *Ann. Geophys.* 10, pp. 103–115.

Crowley, G. (1996). Critical Review of Ionospheric Patches and Blobs. *URSI Review of Radio Science 1993-1996*. Ed. by W. R. Stone. Oxford University Press. ISBN: 978-0-19-856532-1.

Förster, M., S. Rentz, W. Köhler, H. Liu, and S. E. Haaland (2008). IMF Dependence of High-Latitude Thermospheric Wind Pattern Derived from CHAMP Cross-Track Measurements. *Ann. Geophys.* 26.6, pp. 1581–1595. ISSN: 1432-0576. DOI: 10.5194/angeo-26-1581-2008.

Greenwald, R. A., K. B. Baker, J. R. Dudeney, M. Pinnock, T. B. Jones, E. C. Thomas, J.-P. Villain, J.-C. Cerisier, C. Senior, C. Hanuise, R. D. Hunsucker, G. Sofko, J. Koehler, E. Nielsen, R. Pellinen, A. D. M. Walker, N. Sato, and H. Yamagishi (1995). DARN/SuperDARN: A Global View of the Dynamics of High-Latitude Convection. *Space Sci. Rev.* 71 (1-4), pp. 761–796. DOI: 10.1007/BF00751350.

Gustafsson, G., N. E. Papitashvili, and V. O. Papitashvili (1992). A Revised Corrected Geomagnetic Coordinate System for Epochs 1985 and 1990. *J. Atmos. Terr. Phys.* 54.11, pp. 1609–1631. ISSN: 0021-9169. DOI: 10.1016/0021-9169(92)90167-J.

Hedin, A. E. (1987). MSIS-86 Thermospheric Model. *J. Geophys. Res. Space Phys.* 92 (A5), pp. 4649–4662. ISSN: 2156-2202. DOI: 10.1029/JA092iA05p04649.

Hedin, A. E. (1991). Extension of the MSIS Thermosphere Model into the Middle and Lower Atmosphere. *J. Geophys. Res.* 96 (A2), pp. 1159–1172. ISSN: 2156-2202. DOI: 10.1029/90JA02125.

Hinteregger, H. E., L. A. Hall, and G. Schmidtke (1965). Solar XUV Radiation and Neutral Particle Distribution in July 1963 Thermosphere. Fifth International

Space Science Symposium. Amsterdam: North-Holland Publishing Company, pp. 1175–1190.

Hubert, B., S. E. Milan, A. Grocott, C. Blockx, S. W. H. Cowley, and J.-C. Gérard (2006). Dayside and Nightside Reconnection Rates Inferred from IMAGE FUV and Super Dual Auroral Radar Network Data. *J. Geophys. Res.* 111 (A3). 00049, A03217. ISSN: 2156-2202. DOI: 10.1029/2005JA011140.

Hughes, W. J. (1995). The Magnetopause, Magnetotail, and Magnetic Reconnection. *Introduction To Space Physics*. Cambridge, UK: Cambridge University Press, pp. 227–287. ISBN: 0-521-45714-9.

Jacobsen, K. S. and J. I. Moen (2010). On the Correlation between Broad-Band ELF Wave Power and Ion Fluxes in the Cusp. *Ann. Geophys.* 28.6, pp. 1249–1261. ISSN: 1432-0576. DOI: 10.5194/angeo-28-1249-2010.

Vallance Jones, A. (1974). Aurora. Vol. 9. Geophysics and Astrophysics Monographs. Dordrecht: Springer Netherlands. 303 pp. ISBN: 978-94-010-2099-2. DOI: 10.1007/978-94-010-2099-2.

Kamiyama, H. (1966). Ionization and Excitation by Precipitating Electrons. *Rep. Ionos. Sp. Res. Japan* 20, pp. 171–187.

Kamiyama, H. (1967). The Electron Density Distribution in the Lower Ionosphere Produced through Impact Ionization by Precipitating Electrons and through Photoionization by the Associated Bremsstrahlung X-Rays. *J. Geomagn. Geoelectr.* 19.1, pp. 27–47. DOI: 10.5636/jgg.19.27.

Kintner, P. M., J. Franz, P. Schuck, and E. Klatt (2000). Interferometric Coherency Determination of Wavelength or What Are Broadband ELF Waves? *J. Geophys. Res. Space Phys.* 105 (A9). 00049, pp. 21237–21250. ISSN: 2156-2202. DOI: 10.1029/1999JA000323.

Kivelson, M. G. and C. T. Russell, eds. (1995). Introduction To Space Physics. Cambridge, UK: Cambridge University Press. ISBN: 0-521-45714-9.

Kivelson, M. G. (1995). Physics of Space Plasmas. *Introduction To Space Physics*. Cambridge, UK: Cambridge University Press, pp. 27–57. ISBN: 0-521-45714-9.

Kvifte, G. and L. Vegard (1947). On the Emission of the Forbidden Lines from the Metastable Groundstates $^1S_0$ and $^1D_2$ of the Neutral Oxygen Atom. *Geofys. Publ. Geophys. Nor.* XVII.1, pp. 1–35.

Lehtinen, M. S. and A. Huuskonen (1996). General Incoherent Scatter Analysis and GUISDAP. *J. Atmos. Terr. Phys.* Selected papers from the sixth international Eiscat Workshop 58.1, pp. 435–452. ISSN: 0021-9169. DOI: 10.1016/0021-9169(95)00047-X.

Lockwood, M., J. H. W. Jr, T. E. Moore, J. F. E. Johnson, and C. R. Chappell (1985a). A New Source of Suprathermal O+ Ions Near the Dayside Polar Cap Boundary. *J. Geophys. Res.* 90 (A5), pp. 4099–4116. DOI: 10.1029/JA090iA05p04099.

Lockwood, M., M. O. Chandler, J. L. Horwitz, J. H. Waite, T. E. Moore, and C. R. Chappell (1985b). The Cleft Ion Fountain. *J. Geophys. Res. Space Phys.* 90 (A10), pp. 9736–9748. ISSN: 2156-2202. DOI: 10.1029/JA090iA10p09736.

Lockwood, M. and H. C. Carlson (1992). Production of Polar Cap Electron Density Patches by Transient Magnetopause Reconnection. *Geophys. Res. Lett.* 19.17, pp. 1731–1734. ISSN: 1944-8007. DOI: 10.1029/92GL01993.

Lockwood, M., I. W. McCrea, G. H. Millward, R. J. Moffett, and H. Rishbeth (1993a). EISCAT Observations of Ion Composition and Temperature Anisotropy in the High-Latitude F Region. *J. Atmos. Terr. Phys.* 55.6, pp. 895–906. DOI: 10.1016/0021-9169(93)90029-X.

Lockwood, M., W. F. Denig, A. D. Farmer, V. N. Davda, S. W. H. Cowley, and H. Lühr (1993b). Ionospheric Signatures of Pulsed Reconnection at the Earth's Magnetopause. *Nature* 361.6411, pp. 424–428. DOI: 10.1038/361424a0.

Lockwood, M. and M. N. Wild (1993). On the Quasi-Periodic Nature of Magnetopause Flux Transfer Events. *J. Geophys. Res.* 98 (A4), pp. 5935–5940. ISSN: 2156-2202. DOI: 10.1029/92JA02375.

Lorentzen, D. A., P. M. Kintner, J. Moen, F. Sigernes, K. Oksavik, Y. Ogawa, and J. Holmes (2007). Pulsating Dayside Aurora in Relation to Ion Upflow Events during a Northward Interplanetary Magnetic Field (IMF) Dominated by a Strongly Negative IMF B_Y. *J. Geophys. Res. Space Phys.* 112 (A3), A03301. ISSN: 2156-2202. DOI: 10.1029/2006JA011757.

Lühr, H., M. Rother, W. Köhler, P. Ritter, and L. Grunwaldt (2004). Thermospheric Up-Welling in the Cusp Region: Evidence from CHAMP Observations. *Geophys. Res. Lett.* 31.6, p. L06805. ISSN: 1944-8007. DOI: 10.1029/2003GL019314.

Lühr, H. and S. Marker (2013). High-Latitude Thermospheric Density and Wind Dependence on Solar and Magnetic Activity. *Climate and Weather of the Sun-Earth System (CAWSES)*. Springer Atmospheric Sciences. Dordrecht: Springer Netherlands, pp. 189–205. ISBN: 978-94-007-4348-9. DOI: 10.1007/978-94-007-4348-9_11.

Maeda, S., Y. Ogawa, K. Hosokawa, S. Nozawa, S.-i. Oyama, T. Tsuda, and A. Brekke (2009). Ion Heating in High-Speed Flow Channel within the Duskside Cell of the Polar Cap Ion Convection under Large IMF-B_y Condition. *J. Geophys. Res.* 114 (A11), A11307. ISSN: 2156-2202. DOI: 10.1029/2009JA014300.

McCrea, I. W., M. Lester, T. R. Robinson, J.-P. St.-Maurice, N. M. Wade, and T. B. Jones (1993). Derivation of the Ion Temperature Partition Coefficient B‖ from the Study of Ion Frictional Heating Events. *J. Geophys. Res.* 98 (A9), pp. 15701–15715. ISSN: 2156-2202. DOI: 10.1029/92JA02776.

Milan, S. E. (2004). Dayside and Nightside Contributions to the Cross Polar Cap Potential: Placing an Upper Limit on a Viscous-like Interaction. *Ann. Geophys.* 22.10. 00032, pp. 3771–3777. ISSN: 1432-0576. DOI: 10.5194/angeo-22-3771-2004.

Milan, S. E. (2013). Modeling Birkeland Currents in the Expanding/Contracting Polar Cap Paradigm. *J. Geophys. Res. Space Physics* 118.9. 00014, pp. 5532–5542. ISSN: 2169-9402. DOI: 10.1002/jgra.50393.

Moen, J., P. E. Sandholt, M. Lockwood, W. F. Denig, U. P. Løvhaug, B. Lybekk, A. Egeland, D. Opsvik, and E. Friis-Christensen (1995). Events of Enhanced Convection and Related Dayside Auroral Activity. *J Geophys Res* 100 (A12), pp. 23917–23934. DOI: 10.1029/95JA02585.

Moen, J., H. C. Carlson, and P. E. Sandholt (1999). Continuous Observation of Cusp Auroral Dynamics in Response to an IMF B_Y Polarity Change. *Geophys. Res. Lett.* 26.9, pp. 1243–1246. DOI: 10.1029/1999GL900224.

Moen, J., K. Oksavik, and H. C. Carlson (2004a). On the Relationship between Ion Upflow Events and Cusp Auroral Transients. *Geophys. Res. Lett.* 31, p. L11808. DOI: 10.1029/2004GL020129.

Moen, J., M. Lockwood, K. Oksavik, H. C. Carlson, W. F. Denig, A. P. van Eyken, and I. W. McCrea (2004b). The Dynamics and Relationships of Precipitation, Temperature and Convection Boundaries in the Dayside Auroral Ionosphere. *Ann. Geophys.* 22.6, pp. 1973–1987. ISSN: 1432-0576. DOI: 10.5194/angeo-22-1973-2004.

Moen, J., N. Gulbrandsen, D. A. Lorentzen, and H. C. Carlson (2007). On the MLT Distribution of F-Region Polar Cap Patches at Night. *Geophys. Res. Lett.* 34. DOI: 10.1029/2007/GL029632.

Moen, J., Y. Rinne, H. C. Carlson, K. Oksavik, R. Fujii, and H. Opgenoorth (2008). On the Relationship between Thin Birkeland Current Arcs and Reversed Flow Channels in the Winter Cusp/Cleft Ionosphere. *J. Geophys. Res. Space Physics* 113 (A9), A09220. ISSN: 2156-2202. DOI: 10.1029/2008JA013061.

Newell, P. T. and C.-I. Meng (1992). Mapping the Dayside Ionosphere to the Magnetosphere According to Particle Precipitation Characteristics. *Geophys. Res. Lett.* 19.6, pp. 609–612. ISSN: 00948276. DOI: 10.1029/92GL00404.

Newell, P. T., J. M. Ruohoniemi, and C.-I. Meng (2004). Maps of Precipitation by Source Region, Binned by IMF, with Inertial Convection Streamlines. *J. Geophys. Res.* 109 (A10), A10206. ISSN: 2156-2202. DOI: 10.1029/2004JA010499.

Nygrén, T. (1996). Introduction To Incoherent Scatter Measurements. Invers. ISBN: 951-97489-0-3.

Ogawa, Y., S. C. Buchert, R. Fujii, S. Nozawa, and A. P. van Eyken (2009). Characteristics of Ion Upflow and Downflow Observed with the European Incoherent Scatter Svalbard Radar. *J. Geophys. Res.* 114 (A5), A05305. ISSN: 2156-2202. DOI: 10.1029/2008JA013817.

Oksavik, K., J. Moen, and H. C. Carlson (2004). High-Resolution Observations of the Small-Scale Flow Pattern Associated with a Poleward Moving Auroral Form in the Cusp. *Geophys. Res. Lett.* 31, p. L11807. DOI: 10.1029/2004GL019838.

Oksavik, K., J. Moen, H. C. Carlson, R. A. Greenwald, S. E. Milan, M. Lester, W. F. Denig, and R. J. Barnes (2005). Multi-Instrument Mapping of the Small-Scale Flow Dynamics Related to a Cusp Auroral Transient. *Ann. Geophys.* 23.7, pp. 2657–2670. ISSN: 1432-0576. DOI: 10.5194/angeo-23-2657-2005.

Pécseli, H. L. (2005). Selected Topics in Plasma Physics. Compendium.

Picone, J. M., A. E. Hedin, D. P. Drob, and A. C. Aikin (2002). NRLMSISE-00 Empirical Model of the Atmosphere: Statistical Comparisons and Scientific Issues. *J. Geophys. Res. Space Phys.* 107 (A12), SIA 15–1–SIA 15–16. ISSN: 2156-2202. DOI: 10.1029/2002JA009430.

Provan, G., T. K. Yeoman, S. E. Milan, J. M. Ruohoniemi, and R. Barnes (2002). An Assessment of the "map-Potential" and "beam-Swinging" Techniques for Measuring the Ionospheric Convection Pattern Using Data from the SuperDARN Radars. *Ann Geophys* 20.2, pp. 191–202. DOI: 10.5194/angeo-20-191-2002.

Richmond, A. (1987). The Ionosphere. *The Solar Wind And The Earth*. Vol. 30. Geophysics and Astrophysics Monographs. Terra Sci. Publ. Co., pp. 123–140. ISBN: 978-90-277-2472-4.

Rinne, Y., J. Moen, K. Oksavik, and H. C. Carlson (2007). Reversed Flow Events in the Winter Cusp Ionosphere Observed by the European Incoherent Scatter (EISCAT) Svalbard Radar. *J. Geophys. Res. Space Physics* 112 (A10), A10313. ISSN: 2156-2202. DOI: 10.1029/2007JA012366.

Rinne, Y., J. Moen, H. C. Carlson, and M. R. Hairston (2010). Stratification of East-West Plasma Flow Channels Observed in the Ionospheric Cusp in Response to

IMF B_Y Polarity Changes. *Geophys. Res. Lett.* 37.13, p. L13102. ISSN: 1944-8007. DOI: 10.1029/2010GL043307.

Rinne, Y., J. Moen, J. B. H. Baker, and H. C. Carlson (2011). Convection Surrounding Mesoscale Ionospheric Flow Channels. *J. Geophys. Res.* 116 (A5), A05213. ISSN: 2156-2202. DOI: 10.1029/2010JA015997.

Sandholt, P. E., C. S. Deehr, A. Egeland, B. Lybekk, R. Viereck, and G. J. Romick (1986). Signatures in the Dayside Aurora of Plasma Transfer from the Magnetosheath. *J. Geophys. Res.* 91 (A9), pp. 10, 063–10, 079. DOI: 10.1029/JA091iA09p10063.

Sandholt, P. E., B. Lybekk, A. Egeland, R. Nakamura, and T. Oguti (1989). Midday Auroral Breakup. *J. Geomagn. Geoelectr.* 41.4, pp. 371–387. ISSN: 0022-1392. DOI: 10.5636/jgg.41.371.

Sandholt, P. E., M. Lockwood, T. Oguti, S. W. H. Cowley, K. S. C. Freeman, B. Lybekk, A. Egeland, and D. M. Willis (1990). Midday Auroral Breakup Events and Related Energy and Momentum Transfer from the Magnetosheath. *J. Geophys. Res.* 95 (A2), pp. 1039–1060. DOI: 10.1029/JA095iA02p01039.

Sandholt, P. E. and M. Lockwood (1990). Periodic Auroral Events at the High-Latitude Convection Reversal in the 16 MLT Region. *Geophys. Res. Lett.* 17.11, pp. 1877–1880. ISSN: 1944-8007. DOI: 10.1029/GL017i011p01877.

Sandholt, P. E., J. Moen, A. Rudland, D. Opsvik, W. F. Denig, and T. Hansen (1993). Auroral Event Sequences at the Dayside Polar Cap Boundary for Positive and Negative Interplanetary Magnetic Field B_Y. *J. Geophys. Res.* 98 (A5), pp. 7737–7755. ISSN: 2156-2202. DOI: 10.1029/92JA02256.

Sandholt, P. E., C. J. Farrugia, L. F. Burlaga, J. A. Holtet, J. Moen, B. Lybekk, B. Jacobsen, D. Opsvik, A. Egeland, R. Lepping, A. J. Lazarus, T. Hansen, A. Brekke, and E. Friis-Christensen (1994). Cusp/Cleft Auroral Activity in Relation to Solar Wind Dynamic Pressure, Interplanetary Magnetic Field B_Z and B_Y. *J. Geophys. Res.* 99 (A9), pp. 17323–17342. ISSN: 2156-2202. DOI: 10.1029/94JA00679.

Sandholt, P. E., C. J. Farrugia, J. Moen, Ø. Noraberg, B. Lybekk, T. Sten, and T. Hansen (1998). A Classification of Dayside Auroral Forms and Activities as a Function of Interplanetary Magnetic Field Orientation. *J. Geophys. Res.* 103 (A10), pp. 23, 325–23, 345. DOI: 10.1029/98JA02156.

Sandholt, P. E., H. C. Carlson, and A. Egeland (2002). Dayside and Polar Cap Aurora. Vol. 270. Astrophysics and Space Science Library. Kluwer Academic Publishers Group. 287 pp. ISBN: 978-1-4020-0447-6. DOI: 10.1007/0-306-47969-9.

Schunk, R. W. and A. F. Nagy (2009). Ionospheres: Physics, Plasma Physics, and Chemistry. 2nd ed. Cambridge Atmospheric and Space Science Series. Cambridge University Press. ISBN: 0-521-87706-7.

Semeter, J., C. J. Heinselman, J. P. Thayer, R. A. Doe, and H. U. Frey (2003). Ion Upflow Enhanced by Drifting F-Region Plasma Structure along the Nightside Polar Cap Boundary. *Geophys. Res. Lett.* 30.22, p. 2139. ISSN: 0094-8276. DOI: 10.1029/2003GL017747.

Shepherd, S. G. (2014). Altitude-Adjusted Corrected Geomagnetic Coordinates: Definition and Functional Approximations. *J. Geophys. Res. Space Physics* 119.9, pp. 7501–7521. ISSN: 2169-9402. DOI: 10.1002/2014JA020264.

Sigernes, F., M. Dyrland, P. Brekke, S. Chernouss, D. A. Lorentzen, K. Oksavik, and C. Deehr (–0022–2011). Two Methods to Forecast Auroral Displays. *Two Methods to Forecast Auroral Displays*. 38th Annual European Meeting on Atmospheric Studies by Optical Methods. Siuntio Wellness and Conference Resort, Finland.

Skjæveland, Å., J. I. Moen, and H. C. Carlson (2011). On the Relationship between Flux Transfer Events, Temperature Enhancements and Ion Upflow Events in the Cusp Ionosphere. *J. Geophys. Res.* A10305. DOI: 10.1029/2011JA016480.

Skjæveland, Å., J. Moen, and H. C. Carlson (2014). Which Cusp Upflow Events Can Possibly Turn into Outflows? *J. Geophys. Res. Space Physics* 119.8, 2013JA019495. ISSN: 2169-9402. DOI: 10.1002/2013JA019495.

Skjæveland, Å. S., H. C. Carlson, and J. Moen (2017). A Statistical Survey of Heat Input Parameters into the Cusp Thermosphere. Submitted to Journal of Geophysical Research Space Physics.

Southwood, D. J. (1987). The Ionospheric Signature of Flux Transfer Events. *J. Geophys. Res. Space Phys.* 92 (A4), pp. 3207–3213. ISSN: 2156-2202. DOI: 10.1029/JA092iA04p03207.

St.-Maurice, J.-P. and R. W. Schunk (1977). Auroral Ion Velocity Distributions for a Polarization Collision Model. *Planet. Space Sci.* 25.3, pp. 243–260. ISSN: 0032-0633. DOI: 10.1016/0032-0633(77)90135-0.

St.-Maurice, J.-P. and W. B. Hanson (1982). Ion Frictional Heating at High Latitudes and Its Possible Use for an in Situ Determination of Neutral Thermospheric Winds and Temperatures. *J. Geophys. Res. Space Physics* 87 (A9), pp. 7580–7602. ISSN: 2156-2202. DOI: 10.1029/JA087iA09p07580.

Thayer, J. P. and J. Semeter (2004). The Convergence of Magnetospheric Energy Flux in the Polar Atmosphere. *J. Atmos. Sol.-Terr. Phy.* 66.10, pp. 807–824. ISSN: 1364-6826. DOI: 10.1016/j.jastp.2004.01.035.

Thébault, E., C. C. Finlay, C. D. Beggan, P. Alken, J. Aubert, O. Barrois, F. Bertrand, T. Bondar, A. Boness, L. Brocco, E. Canet, A. Chambodut, A. Chulliat, P. Coïsson, F. Civet, A. Du, A. Fournier, I. Fratter, N. Gillet, B. Hamilton, M. Hamoudi, G. Hulot, T. Jager, M. Korte, W. Kuang, X. Lalanne, B. Langlais, J.-M. Léger, V. Lesur, F. J. Lowes, S. Macmillan, M. Mandea, C. Manoj, S. Maus, N. Olsen, V. Petrov, V. Ridley, M. Rother, T. J. Sabaka, D. Saturnino, R. Schachtschneider, O. Sirol, A. Tangborn, A. Thomson, L. Tøffner-Clausen, P. Vigneron, I. Wardinski, and T. Zvereva (2015). International Geomagnetic Reference Field: The 12th Generation. *Earth Planets Space* 67.1. ISSN: 1880-5981. DOI: 10.1186/s40623-015-0228-9.

Wahlund, J.-E., H. J. Opgenoorth, I. Häggström, K. J. Winser, and G. O. L. Jones (1992). EISCAT Observations of Topside Ionospheric Ion Outflows during Auroral Activity: Revisited. *J. Geophys. Res.* 97 (A3). 00108, pp. 3019–3037. ISSN: 2156-2202. DOI: 10.1029/91JA02438.

Wannberg, G., I. Wolf, L.-G. Vanhainen, K. Koskenniemi, J. Röttger, M. Postila, J. Markkanen, R. Jacobsen, A. Stenberg, R. Larsen, S. Eliassen, S. Heck, and A. Huuskonen (1997). The EISCAT Svalbard Radar: A Case Study in Modern Incoherent Scatter Radar System Design. *Radio Sci.* 32.6, pp. 2283–2307. ISSN: 1944-799X. DOI: 10.1029/97RS01803.

Yau, A. W. and M. André (1997). Sources of Ion Outflow in the High Latitude Ionosphere. *Space Sci. Rev.* 80.1, pp. 1–25. ISSN: 0038-6308. DOI: 10.1023/A:1004947203046.

Part III

Papers

Chapter 7

Paper 1: On the Relationship between Flux Transfer Events, Temperature Enhancements and Ion Upflow Events in the Cusp Ionosphere

Chapter 8

Paper 2: Which Cusp Upflow Events Can Possibly Turn into Outflows?

Chapter 9

Paper 3: A Statistical Survey of Heat Input Parameters into the Cusp Thermosphere

Appendix A

Corrections

A.1 Correction to Paper 1

The word “outflow” is used incorrectly in sections 4.1 and 4.4 of the paper. The correct word is “upflow”, as the paper does not study outflow, only upflow. While outflow might concievably exist in the ESR’s field of view as a long-tail part of the plasma velocity distribution, it is not visible in this analysis which only shows the average bulk velocity.